Stratification Breakdown in Antarctic Coastal Polynyas. Part II: Influence of an Ice Tongue and Coastline Geometry

YILANG XU,[a,b] WEIFENG (GORDON) ZHANG,[a] TED MAKSYM,[a] RUBAO JI,[c] AND YUN LI[d]

[a] *Applied Ocean Physics and Engineering Department, Woods Hole Oceanographic Institution, Woods Hole, Massachusetts*
[b] *MIT-WHOI Joint Program in Oceanography/Applied Ocean Science and Engineering, Cambridge, Massachusetts*
[c] *Biology Department, Woods Hole Oceanographic Institution, Woods Hole, Massachusetts*
[d] *School of Marine Science and Policy, University of Delaware, Lewes, Delaware*

(Manuscript received 21 October 2022, in final form 10 June 2023, accepted 14 June 2023)

ABSTRACT: This is Part II of a study examining wintertime destratification in Antarctic coastal polynyas, focusing on providing a qualitative description of the influence of ice tongues and headlands, both common geometric features neighboring the polynyas. The model of a coastal polynya used in Part I is modified to include an ice tongue and a headland to investigate their impacts on the dispersal of water formed at the polynya surface, which is referred to as Polynya Source Water (PSW) here. The model configuration qualitatively represents the settings of some coastal polynyas, such as the Terra Nova Bay Polynya. The simulations highlight that an ice tongue next to a polynya tends to break the alongshore symmetry in the lateral return flows toward the polynya, creating a stagnant region in the corner between the ice tongue and polynya where outflow of the PSW in the water column is suppressed. This enhances sinking of the PSW and accelerates destratification of the polynya water column. Adding a headland to the other side of the polynya tends to restore the alongshore symmetry in the lateral return flows, which increases the offshore PSW transport and slows down destratification in the polynya. This work stresses the importance of resolving small-scale geometric features in simulating vertical mixing in the polynya. It provides a framework to explain spatial and temporal variability in rates of destratification and Dense Shelf Water formation across Antarctic coastal polynyas, and helps understand why some polynyas are sources of Antarctic Bottom Water while others are not.

KEYWORDS: Antarctica; Sea ice; Coastal flows; Convection; Oceanic mixed layer; Numerical analysis/modeling

1. Introduction

Antarctic coastal polynyas are sites of strong wintertime vertical mixing due to sea ice formation and brine rejection (Morales Maqueda et al. 2004). Coastal polynyas are complex systems and can vary drastically in their water-column destratification process (Aoki et al. 2020; Silvano et al. 2018). Destratification of the polynya water column is directly affected by changes in local atmospheric and oceanic forcings (Ackley et al. 2020; Le Bel et al. 2021). Investigating the impacts of these local forcings is vital to understanding the variability in timing and rate of the polynya destratification. Part I of this study (Xu et al. 2023, hereafter Part I) uses numerical simulations of an idealized Antarctic coastal polynya to investigate the influence of various physical factors on the polynya destratification process. It shows that wind-driven ocean currents can alter lateral dispersal of the water mass formed at the polynya surface—which we named Polynya Source Water (PSW)—in the water column and affect the strength of vertical mixing in the polynya. In particular, offshore katabatic winds can drive an offshore ocean current, which transports the PSW away from the polynya before it reaches the bottom and thus reduces the polynya destratification rate. In contrast, the alongshore easterly winds can induce onshore Ekman transport, which suppresses the offshore transport of the PSW and enhances vertical mixing in the polynya. Part of the PSW that is dense enough to sink to the bottom becomes Dense Shelf Water (DSW), which flows offshore into the deeper ocean and contributes to the formation of Antarctic Bottom Water (AABW) (Kitade et al. 2014; Ohshima et al. 2013).

Part I does not consider the influence of other factors, such as ice tongues, coastline geometry, seafloor topography, and the intrusion of Circumpolar Deep Water. Many Antarctic coastal polynyas are accompanied by ice tongues located to the immediate east or southeast of the polynya (Nihashi and Ohshima 2015) and complex seafloor topography (e.g., Randall-Goodwin et al. 2015; Snow et al. 2018; Yoon et al. 2020). The neighboring ice tongues block the along-coast drift of sea ice into the polynya and help keep the polynyas open (Bromwich and Kurtz 1984; Kurtz and Bromwich 1985; Massom et al. 1998, 2001). Several ice-tongue-associated polynyas have been identified as sources of AABW, e.g., the Cape Darnley Polynya (Ohshima et al. 2013), the Mertz Polynya (Williams et al. 2010), and the Terra Nova Bay Polynya (e.g., Budillon and Spezie 2000; Rusciano et al. 2013). Some of these studies suggest that AABW formation in these polynyas is subject to the impact of the ice tongues. Consequently, changes in the ice tongues morphology (e.g., length) may alter the AABW production. One example is the calving of the Mertz Glacier Tongue in 2010, which greatly reduced the sea ice productivity in the Mertz Polynya (Tamura et al. 2012). A reduction in AABW formation was observed in the Mertz Polynya region two years after the calving event (Lacarra et al. 2014; Snow et al. 2018). The length of the Mertz Glacier Tongue changes periodically, and multiple calving events have occurred in the past (Giles 2017). This suggests that the sea ice and DSW formation in the Mertz Polynya region may also vary in time following changes in the Mertz Glacier Tongue. Since the Mertz Glacier Tongue is

Corresponding author: Yilang Xu, yilangxu@mit.edu

DOI: 10.1175/JPO-D-22-0219.1

currently growing at a rate of ~1 km yr^{-1} (Giles 2017), a gradual variation of the Mertz Polynya activity is expected in the next several decades with growth of the Mertz Glacier Tongue.

Part II focuses on two influencing factors that are not considered in Part I, ice tongue and coastline geometry, and investigates their influence on the destratification process in Antarctic coastal polynyas. Previous studies (Kurtz and Bromwich 1985; Ohshima et al. 2013; Williams et al. 2010) of the influence of ice tongues on the PSW formation mainly consider the blocking effect of an ice tongue on the advection of sea ice into the polynya, which prolongs the duration of polynya opening and enhances brine rejection at the surface. Since ice tongues are hundreds of meters thick (Stevens et al. 2017), the blocking effect presumably extends deep into the water column and affects the subsurface ocean current in the polynya region. Consequently, PSW circulation in the polynya region may be altered, which, as demonstrated in Part I, could change the destratification rate in the polynya water column. Besides ice tongues, coastline geometry in the vicinity of Antarctic coastal polynyas is usually complex (Nihashi and Ohshima 2015), which might also influence the PSW circulation and destratification process. Because of their small spatial scales, ice tongue and local coastline geometry are often not fully resolved in large-scale ocean models (e.g., Dinniman et al. 2020) and details of their impacts on PSW circulation are largely unknown.

In this work, the Terra Nova Bay Polynya (TNBP; Fig. 1a) is used as a representative example to illustrate the need to consider the influence of ice tongues and coastline geometry, particularly, a neighboring headland, in the analysis of polynya wintertime destratification and PSW circulation. The TNBP is located in the western Ross Sea, between the Drygalski Ice Tongue to the south and a headland named Cape Washington to the north. Similar to the Mertz Glacier Tongue, the length of the Drygalski Ice Tongue has also changed in the past century due to calving events (Frezzotti and Mabin 1994; Parmiggiani and Fragiacomo 2005). During the winter months (April–September), air temperature in this region frequently drops below −20°C (Fig. 2a), and strong katabatic winds from the Nansen Ice Shelf blow offshore (eastward; Fig. 2d), extending beyond the Terra Nova Bay (Bromwich 1989; Wenta and Cassano 2020) and forming the TNBP. The TNBP is characterized by strong sea ice production and DSW formation in winter (Budillon and Spezie 2000; Rusciano et al. 2013). It is sustained by katabatic winds and the Drygalski Ice Tongue, which intrudes ~90 km into the Ross Sea (Indrigo et al. 2020), and blocks sea ice from entering the TNBP from the south (Kurtz and Bromwich 1985).

In May 2017, during the Polynyas, Ice Production, and seasonal Evolution in the Ross Sea (PIPERS) project field campaign (Ackley et al. 2020), researchers observed a rapid deepening of the surface mixed layer in the TNBP (Thompson et al. 2020). Conductivity–temperature–density (CTD) cast in the vicinity of the ice tongue on May 6 showed that the water column was stratified below 100 m (Fig. 3). On 9 May, another CTD cast at the same location showed that temperature and salinity in the upper 500 m had been largely homogenized (Fig. 3). Hence, within three days, the depth of the surface mixed layer had extended from 100 to 500 m. This mixing event took place much faster than the gradual mixing in the Vincennes Bay Polynya, which usually takes several months as revealed by the seal data in Part I. The atmospheric data from Manuela Automatic Weather Station on the coast of the TNBP showed that a katabatic event occurred during the 3-day period between the two CTD casts (Fig. 2b). This extraordinary water-column mixing event was accompanied by intensified offshore sea ice export, as indicated by the sea ice plume in the satellite image taken on 8 May (Fig. 1b).

To highlight the influence of an ice tongue and a headland, satellite images of the TNBP during katabatic events in February and March 2015 are shown in Figs. 1c–h. During this period, sea ice started to accumulate in the TNBP. As the katabatic winds pushed new frazil and pancake ice northeastward away from the polynya, an offshore ice plume and an anticyclonic (counterclockwise) vortex to the north of the TNBP were formed. At the end of February, an iceberg detached from the Nansen Ice Shelf started to move offshore at a speed of ~0.3 m s^{-1} (Figs. 1c,d). It later entered the vortex and kept on moving counterclockwise in the vortex for more than three weeks. The spinning motion of the iceberg in the vortex remained pronounced even during later times when the sea ice cover became thicker (Figs. 1g,h), indicating that the vortex flow pattern still existed under the sea ice cover.

Close examination of the satellite MODIS images shows that this surface pattern of the TNBP circulation occurred in the early winters of all data-available years, 2000–22 (not shown). Meanwhile, wintertime (April–September) winds in the region (Fig. 2a) were strong, frequently falling into the katabatic regime (≥25 m s^{-1}; Rusciano et al. 2013). Analysis of the wind data in 2017 shows that winds at the TNBP oscillated strongly within the frequency band of 2–5 days (Fig. 2c) and that the dominant wind direction was offshore toward the east (Fig. 2d). Such strong offshore winds can presumably sustain the offshore ocean current in the polynya region and the anticyclonic vortex to the immediate north of the polynya, despite the sea ice cover. These ocean circulation patterns likely affect the distribution of newly formed PSW and vertical mixing in the water column of the TNBP.

This study provides a mechanistic understanding of how an ice tongue and a headland could jointly influence water-column destratification in a polynya. Due to complexity in the associated three-dimensional flow, it is difficult to incorporate the influence of an ice tongue or a headland in a quantitative scaling analysis. Instead, Part II of this study focuses on providing a qualitative description of the first-order influence of an ice tongue and a headland. We hypothesize that they affect the wintertime destratification process by altering the polynya circulation and then the PSW dispersal in a polynya. The TNBP is used as an example to guide the model design. But the result should be applicable to other coastal polynyas with similar morphological settings.

2. Model setup

The coastal polynya model used in this study is based on the Massachusetts Institute of Technology General Circulation Model (MITgcm; Marshall et al. 1997) and the details of the modules used in this study are described in Part I. The model has an idealized configuration that spans 22.5° in

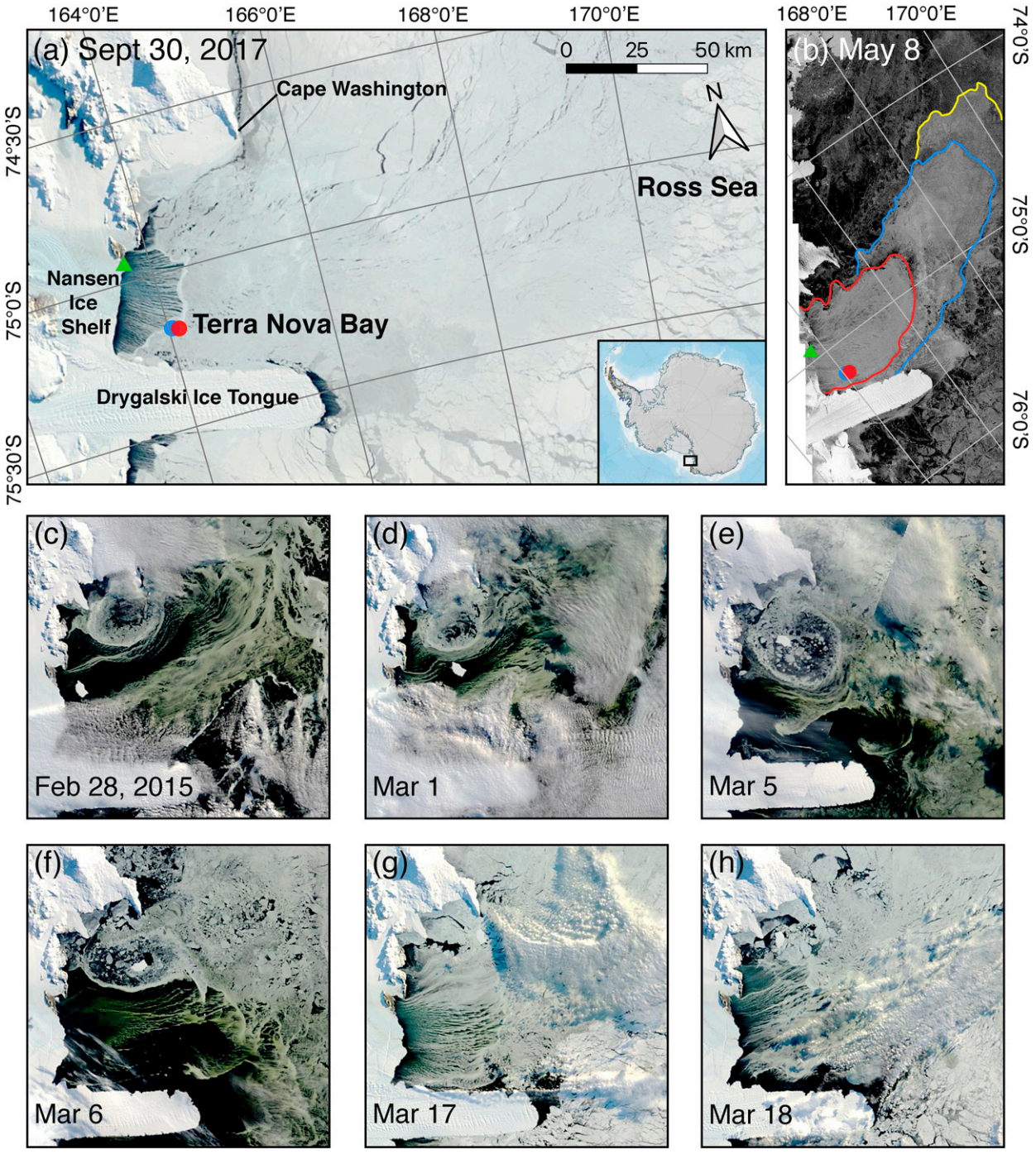

FIG. 1. (a) *Terra*/*Aqua* MODIS satellite image of the Terra Nova Bay Polynya region on 30 Sep 2017. (b) Sentinel-1 SAR satellite image of the Terra Nova Bay Polynya on 8 May 2017. In both (a) and (b), the green triangle locates the Manuela weather station; the blue and red circles denote the locations of PIPERS CTD casts on 6 and 9 May 2017, respectively. Colored lines in (b) outline the offshore boundary of the polynya and outer boundaries of the previous sea ice plume. These images are selected to show a clear (cloud-free) pattern of the polynya surface and its offshore sea ice plume. (c)–(h) *Terra*/*Aqua* MODIS satellite images of the Terra Nova Bay Polynya between 28 Feb and 18 Mar 2015.

longitude and 6° in latitude. It includes a flat bottom of 500 m deep and an ice shelf with a cavity underneath that incises into the continent to the south (Fig. 4). An idealized polynya is formed by an offshore wind blowing from the ice shelf into the ocean. The horizontal grid spacing in the central study area around the polynya is ~1 km, increasing northward toward the open boundaries. The vertical grid is uniform with a layer thickness of 10 m. To track the PSW, passive tracer

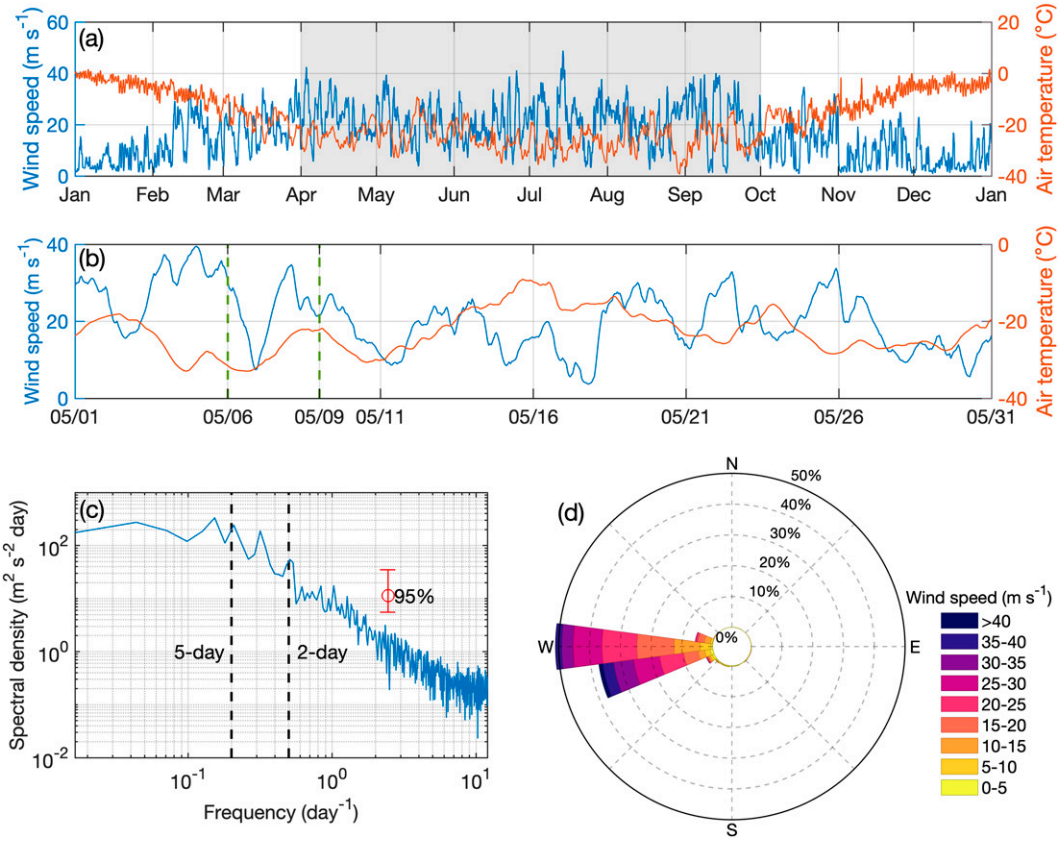

FIG. 2. (a) Wind speed and air temperature measured at the Manuela weather station in 2017; (b) a zoomed-in version of (a) showing the time series in May; (c) spectral density of the measured wind speed; (d) wind rose plots of the wind speed and the direction it comes from in the winter months (April–September). The gray shade in (a) highlights the austral winter months; the green dashed lines in (b) highlight the times of PIPERS CTD casts; the error bar in (c) indicates the 95% confidence interval; dashed lines in (c) denote frequencies corresponding to oscillation periods of 2 and 5 days.

concentration is constantly restored to 1 at the polynya surface where sea ice concentration is below 70%.

In Part II, an ice tongue and a headland are added to the model, while other aspects of the model remain the same as in Part I. The idealized ice tongue is located to the immediate east of the ice shelf opening and the polynya, and has a three-dimensional shape qualitatively similar to the Drygalski Ice Tongue next to the TNBP (Stevens et al. 2017). In particular, the ice tongue is 111 km long (1° in latitude) in the cross-shore direction and 28 km wide in the alongshore direction. Its draft gradually reduces from 400 m on the coast to 0 at its offshore end. In some of the simulations, a headland is placed west of

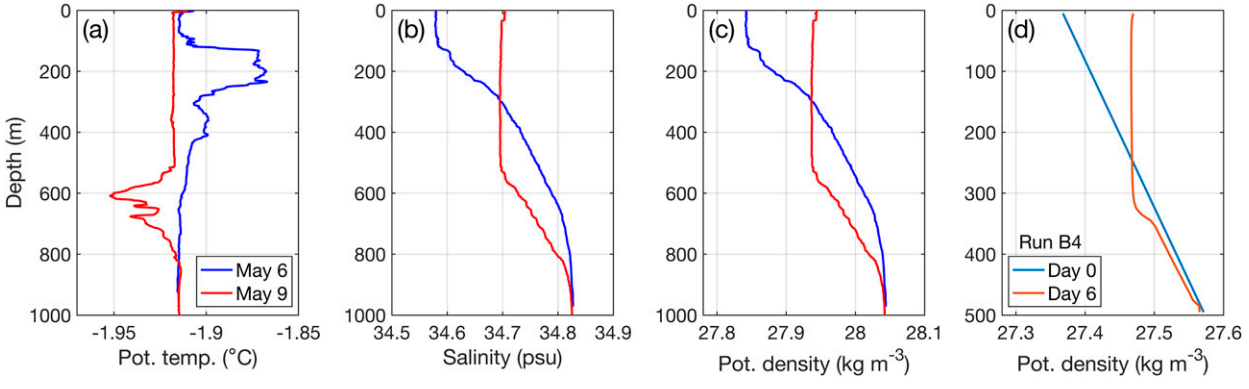

FIG. 3. CTD casts of (a) potential temperature, (b) salinity, and (c) potential density in the Terra Nova Bay Polynya during the PIPERS cruise on 6 and 9 May 2017. The locations of the CTD casts are labeled with circles in Figs. 1a and 1b. (d) Profiles of potential density sampled at the location labeled by the purple circle in the idealized Run B4 (Fig. 6a) on day 0 and 6.

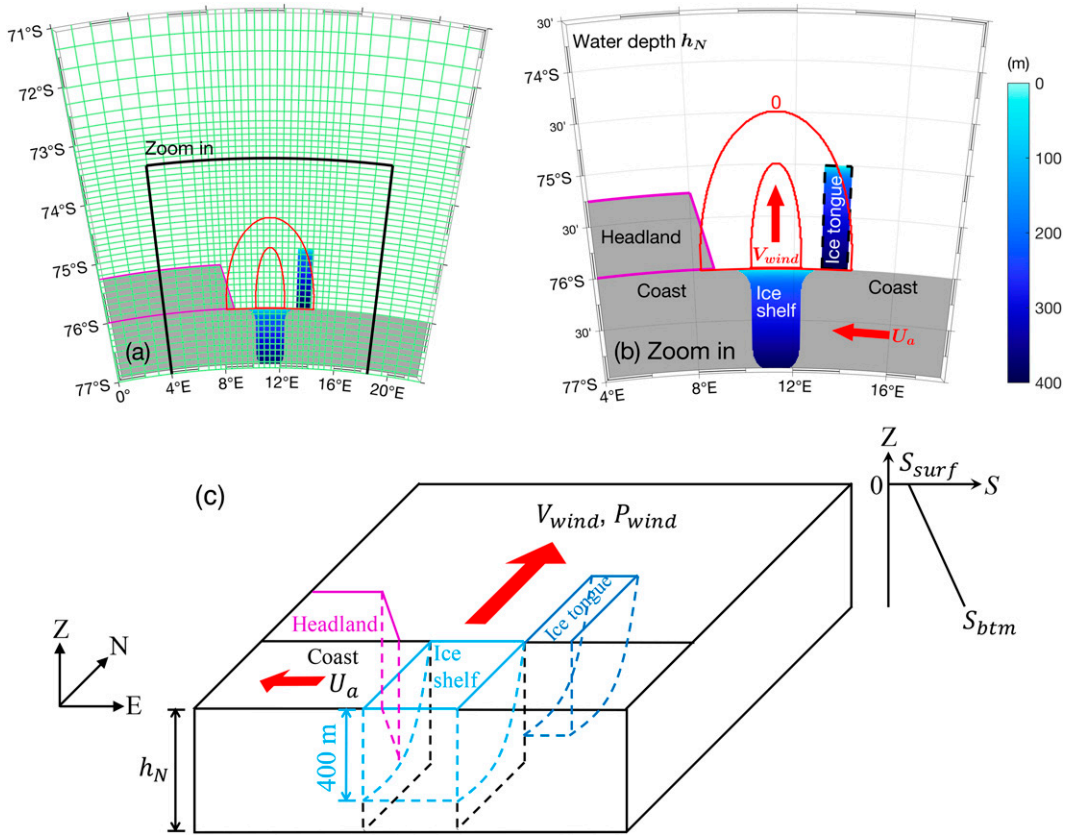

FIG. 4. (a) An aerial view of the model domain and grid and (b) a zoomed-in view of the region marked by black lines in (a). Green lines in (a) depict every 10 horizontal grid cells; the gray regions in (a) and (b) indicate land; the filled color shows the vertical position of the interface between the ice shelf/tongue and ocean, i.e., thickness of the ice shelf/tongue; red ellipses outline regions of the offshore katabatic wind V_{wind} and its inner region of maximum speed; red arrows in (b) indicate the directions of V_{wind} and the alongshore easterly winds U_a in Runs B2, B5, and B6; purple lines in both (a) and (b) denote the shape of the headland; the black dashed line in (b) outlines the lateral boundaries of the ice tongue. (c) A three-dimensional schematic illustration of the model setup and the initial salinity profile.

the ice shelf opening, extending over the whole water column (Fig. 4). This model configuration represents the general setting around some of the Antarctic coastal polynyas, e.g., the TNBP and the Mertz Polynya, including the relative position of the coastline, ice shelf, ice tongue, and katabatic winds. It does not include any small-scale icescape and coastline geometry, or reproduce the orientation of any specific polynya. It also neglects complex seafloor topography. Because this study focuses on capturing the canonical circulation in a representative Antarctic coastal polynya and analyzing the first-order dynamics of an ice tongue and a headland affecting polynya *local* destratification, influences of smaller-scale coastline geometry, ice shelf/tongue morphology, polynya orientation, and seafloor topography are neglected here. Their influence on the polynya circulation and stratification is left for future studies. Note that the directions described in this study refer to those in the model setup and do not necessarily apply to specific polynyas in the ocean. Other factors of the model, such as initial stratification, offshore winds, and alongshore winds, are kept the same as the base runs in Part I. This consistency in the model setup allows for a direct comparison of the model results to examine the influences of the ice tongue and headland. This choice is also supported by the fact that katabatic winds at some Antarctic coastal polynyas show similar characteristics (e.g., speed and fluctuation frequencies), as indicated by winds observed at the TNBP (Fig. 2) and the Vincennes Bay Polynya (Fig. 2 in Part I).

A total of six base model runs, B1–6, are analyzed in this study. Runs B1 and B2 have been examined in Part I. Runs B3–6 are modified from B1 with the addition of an ice tongue, a headland and alongshore easterly wind with the speed of U_a (Table 1). B3 is the same as B1, except for the addition of an ice tongue of

TABLE 1. Base runs and their difference from B1.

Run labels	U_a (m s^{-1})	Ice tongue length	Headland
B1	0	0	No
B2	10	0	No
B3	0	Full length: 111 km	No
B3-IT	0	11–100 km	No
B4	0	Full length: 111 km	Yes
B5	10	Full length: 111 km	No
B6	10	Full length: 111 km	Yes

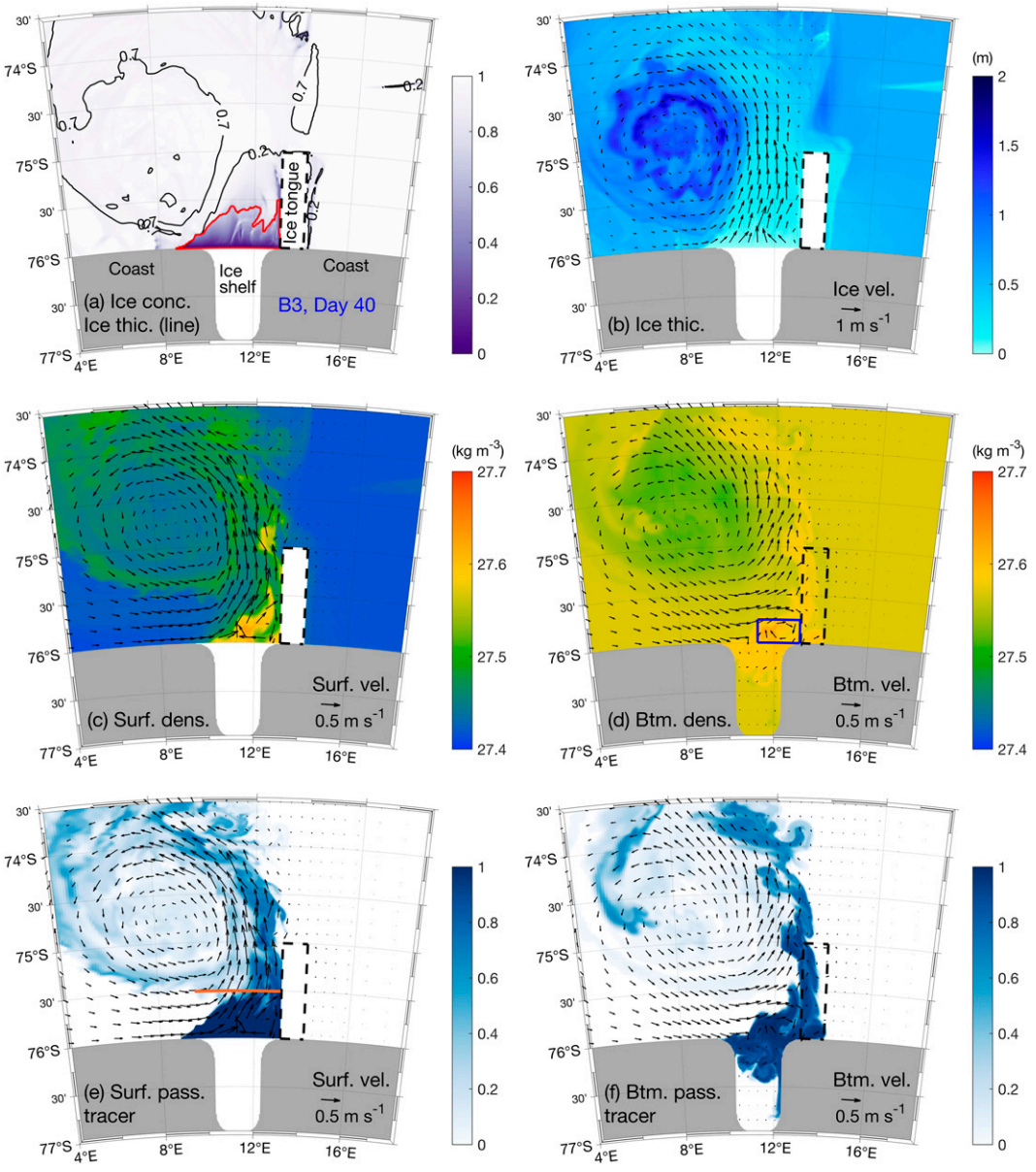

FIG. 5. Snapshots of model fields on day 40 from Run B3: (a) sea ice concentration (color) and thickness (black contours in meters); (b) sea ice thickness (color) and sea ice velocity (arrows); potential density (color) and velocity (arrows) at the (c) surface and (d) bottom; concentration of passive tracer (color) originating from the polynya surface and velocity (arrows) at the (e) surface and (f) bottom. The red line in (a) outlines the coastal polynya on day 40; the orange line in (e) indicates the transect where offshore fluxes are integrated vertically and zonally and shown in Fig. 16; the blue box in (d) indicates the ice tongue end corner region where the surface and bottom densities are averaged and shown in Fig. 11.

111 km long. To consider the influence of the ice tongue length, a set of nine runs, B3-IT, with different ice tongue length (11–100 km) are performed. Other factors in B3-IT are the same as in B3. B4 includes both an ice tongue and a headland, and is qualitatively similar to the setting of the TNBP. Results of the B4 simulation will be qualitatively compared to observations in the TNBP during wintertime katabatic events. B5 and B6 are the same as B3 and B4, respectively, except with the addition of alongshore easterly winds. Their comparisons will reveal how alongshore winds interact with complex coastal geometry and modify the polynya destratification process.

3. Results

a. General pattern of modeled polynyas

Snapshots of sea ice concentration and thickness, potential density, and passive tracer concentration on model day 40 (Figs. 5 and 6) show that a coastal polynya is formed at the

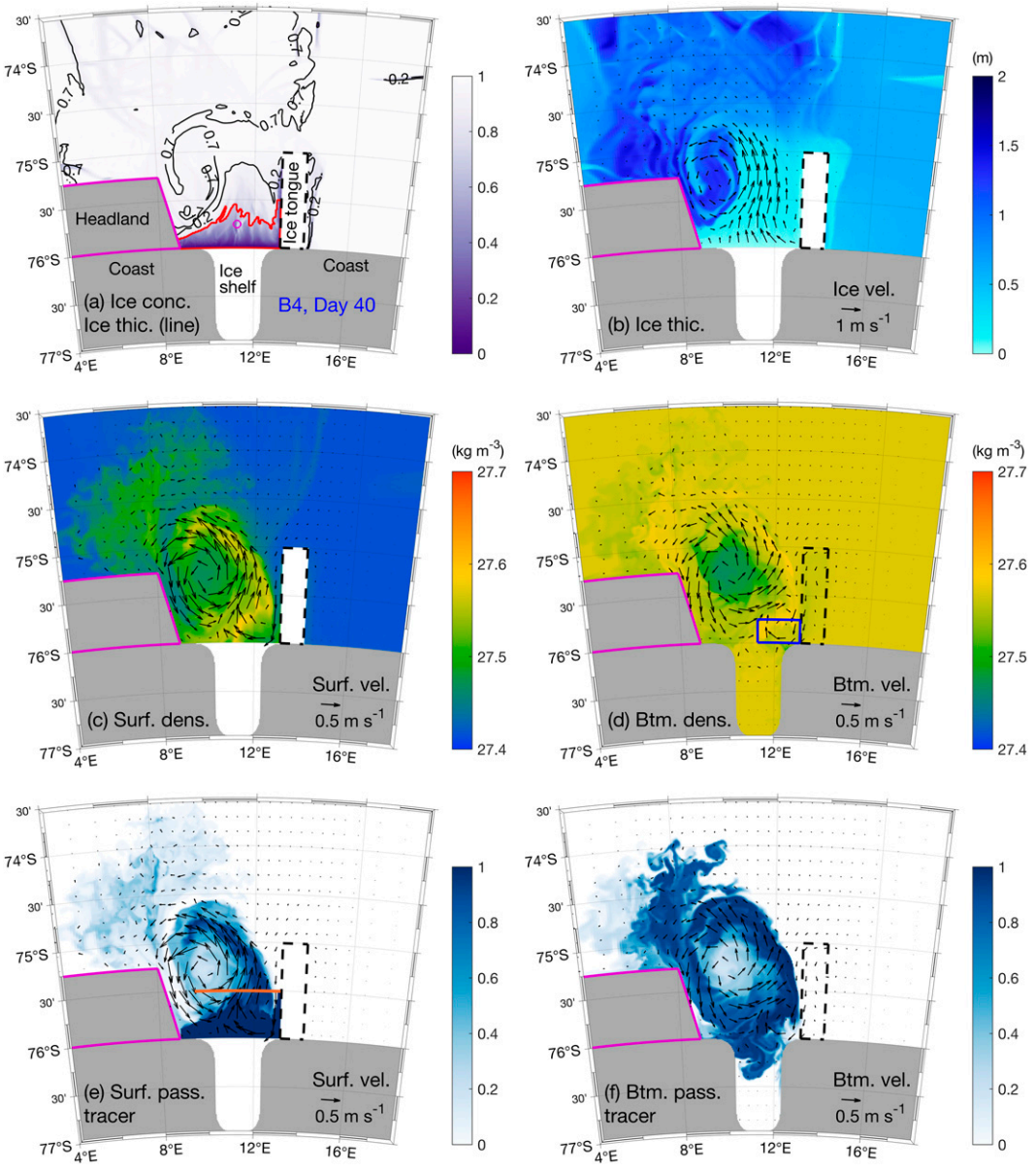

FIG. 6. Snapshots of model fields on day 40 from Run B4: (a) sea ice concentration (color) and thickness (black contours in meters); (b) sea ice thickness (color) and sea ice velocity (arrows); potential density (color) and velocity (arrows) at the (c) surface and (d) bottom; concentration of passive tracer (color) originating from the polynya surface and velocity (arrows) at the (e) surface and (f) bottom. The red line in (a) outlines the coastal polynya on day 40; the purple circle in (a) denotes the location of potential density plotted in Fig. 3d; the orange line in (e) indicates the transect where fluxes are integrated vertically and zonally and shown in Fig. 16; the blue box in (d) indicates the ice tongue end corner region where the surface and bottom densities are averaged and shown in Fig. 11.

center of the wind field at the ice shelf front in both Runs B3 and B4. Meanwhile, their sea ice and ocean fields differ drastically and also deviate significantly from the patterns in B1 (Fig. 5 in Part I). To validate the model, we qualitatively compare modeled fields in B4 on day 40 (representative of the early winter condition) with observed sea ice and ocean conditions. Run B4 is chosen here because its configuration qualitatively resembles the TNBP.

Because the polynya system is largely forced by winds, applying representative atmospheric conditions and reliable air–sea interaction parameterization is important for the success of the model simulations. Thus, we here provide a qualitative model validation by comparing modeled surface heat fluxes with those observed in the TNBP during the PIPERS expedition in May 2017 (Guest 2021), even though the atmospheric and ocean conditions in the idealized model do not exactly

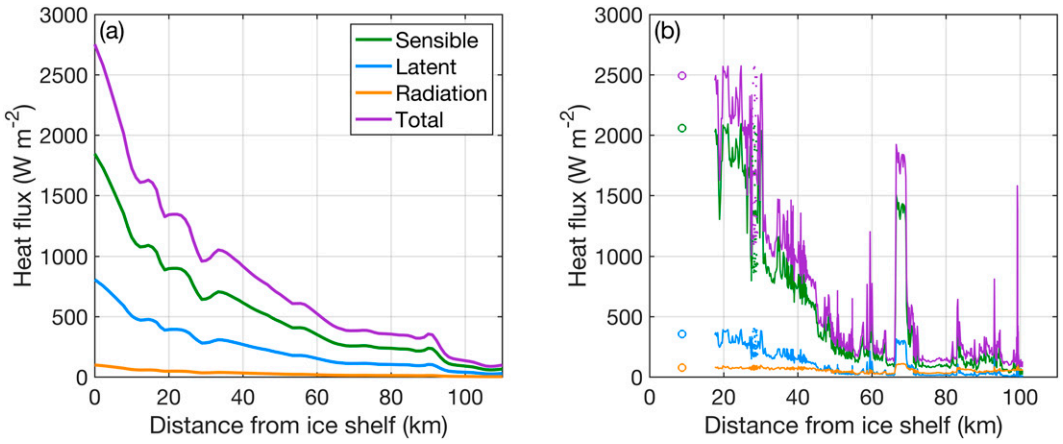

FIG. 7. (a) Snapshots of modeled surface heat fluxes out of the ocean along the cross-shore centerline of the ice shelf in Run B4 on day 40, as a function of the distance from the ice shelf. Positive values indicate heat loss from the ocean. (b) Surface heat fluxes measured in the Terra Nova Bay Polynya on 8 May 2017 (Guest 2021).

match the condition during the observation. The comparison (Fig. 7) shows that the model captures general trends of the observed heat fluxes along the centerline of the polynya, including the overall magnitude of the fluxes, their relative contributions, and their cross-polynya distributions. In particular, both the model and observations show the dominance of sensible heat flux, followed by latent flux and radiation flux. All fluxes have the highest magnitude in the ice shelf front region where the total heat flux reaches about 2500 W m^{-2}, and they all decrease gradually offshore. The highest fluxes occur in the ice shelf front region because the katabatic winds are the strongest and the sea ice concentration is the lowest there, both of which enhance the heat exchange between the air and ocean. Further offshore, the katabatic wind speed remains high, but sea ice concentration and thickness increase due to freezing and compression, and sea ice hinders the air–sea heat exchange. Note that small-scale variabilities in the observed fluxes are presumably caused by ice floes or leads (Guest 2021), which are not resolved by the model. The general agreement between the modeled and observed heat fluxes confirms that the prescribed surface forcings and the air–sea interaction parameterization in the model reasonably capture key features of the polynya forcings.

The model produces an offshore-flowing plume and a vortex pattern in the sea ice fields (Fig. 6b), similar to those shown in the satellite images (Figs. 1c–h). This indicates that the model qualitatively captures the wind-driven sea ice and ocean flows on the surface. Below the surface, the model captures the deepening of the surface mixed layer within a few days of a katabatic wind event (Fig. 3d). In particular, water density in the initially stratified top 300 m is homogenized on day 6. This pattern also qualitatively resembles the deepening of the surface mixing layer on 6–9 May 2017. These demonstrate the model's capability in capturing key sea ice and ocean dynamics in Antarctic coastal polynyas as represented by the TNBP, allowing us to diagnose the underlying dynamics of polynya circulation from the simulations.

In B1, in the absence of an ice tongue and a headland, a sea ice and PSW plume driven by the katabatic winds flows northward offshore in the polynya region (Fig. 5 in Part I). The plume gradually turns to its left under the influence of the Coriolis force. To compensate for the plume offshore transport, an eastward (westward) current toward the polynya is formed on the coast to the west (east) of the polynya. To the far west and east of the plume, the flow is weakly southward, which, together with the coastal currents and the plume outflow, forms a weak anticyclonic (cyclonic) flow pattern with a radius of 100–150 km to the west (east) of the plume. Together, they form a dipole flow pattern that persists deep into the water column.

In B3, with the addition of an ice tongue, the relatively symmetric flow patterns in the alongshore direction break down, and the ice tongue blocks sea ice and ocean circulation to the east side of the polynya (Figs. 5b–d). Yet on the west side, the wind stress shear induces an anticyclonic vortex in sea ice and ocean fields. The plume outflow can be considered as the eastern edge of the vortex. Compared to the anticyclonic flow pattern in B1, the anticyclonic vortex in B3 is stronger and shifted slightly to the east. The maximum surface and bottom flow speeds in the anticyclonic vortex in B3 are ~0.5 and ~0.3 m s^{-1}, respectively. Examination of the temporal evolution of the model field reveals that sea ice is gradually entrained into the vortex and converges toward the vortex center forming thicker ice there (Fig. 5b). Meanwhile, some PSW is transported offshore away from the polynya throughout the water column (Figs. 5e,f). On day 40, high-density water appears on the bottom at the corner of the ice tongue and ice shelf (blue box in Fig. 5d; hereafter referred to as "ice tongue end corner") and within the ice shelf cavity (Fig. 5f), indicating that the PSW has already penetrated through the entire water column reaching the bottom. Therefore, the water column of part of the polynya region has been completely mixed on day 40. This is much faster than the case without the ice tongue (B1), where it takes the PSW more than 100 days to reach the bottom.

In B4, with an ice tongue and a headland, the patterns of sea ice distribution and ocean circulation on day 40 differ from those in B1 and B3. Specifically, the headland to the west of the polynya suppresses the lateral compensating flow from the west, while the ice tongue to the east of the polynya blocks the sea ice and ocean flows on the east side. A compact anticyclonic vortex is formed to the northwest of the polynya with a radius of ~50 km, smaller than the vortex formed in B3 without the headland. The maximum surface and bottom flow speeds in the vortex in B4 are ~1 and ~0.5 m s^{-1}, respectively, higher than those in B1 and B3. The shrinking of the vortex and strengthening of the vortex flow in B4 is caused by the headland. The dynamics of the vortex formation will be discussed in section 3b. Part of the PSW is entrained into the vortex, and a portion of that PSW reenters the polynya region through the eastward compensating flow to the west of the polynya. While the PSW concentration remains low at the center of the vortex on day 40 (Figs. 6e,f), the bottom density at the vortex center is similar to that at the surface (Figs. 6c,d), lower than the surrounding region. This indicates that the low-density, low-salinity surface water has been subducted at the vortex center. Relative to B3, B4 shows lower bottom density at the ice tongue end corner on day 40, suggesting slower PSW sinking and polynya water-column destratification.

Both B3 and B4 show a much faster destratification in the polynya region than B1. This difference is more pronounced later in the simulations, such as on day 100 (Fig. 8), when both surface and bottom density fields differ greatly among these three runs. While the PSW has barely reached the polynya bottom in B1 on day 100, in B3, a substantial amount of PSW has sunk to the bottom and occupied the ice shelf cavity. The bottom density in B4 is higher than that B1, but lower than in B3. Volume integrations of the modeled PSW passive tracer show that the amount of PSW residing in the ice shelf cavity on day 100 reduces from B3 to B4 by 27%.

Another difference among B1, B3, and B4 is the PSW circulation in the polynya water column. In B1, PSW mainly moves directly offshore of the polynya. In contrast, PSW stays near the ice tongue end corner in B3, while it spreads out in the polynya region in B4. This is illustrated in the cross-shore transects at the polynya's west end, middle, and east end (Fig. 9) and the alongshore transect near the coast (Fig. 10). In B1 on day 100, much of the PSW is diffusively distributed in the water column north of the polynya (Fig. 9b); in B3, more PSW appears in the water column below the polynya on the middle and eastern cross-shore transects close to the ice tongue (Figs. 9d–f); in B4, the PSW is more uniformly distributed on the three cross-shore transects (Figs. 9g–i). The middle transects also show more PSW intruding into the ice shelf cavity in B3 than in B4 and B1 (Figs. 9b,e,h); the eastern transects show more offshore fresher (less dense) water intruding onshore toward the polynya in B4 than that in B3 (Figs. 9f,i). The along-coast transects near the ice shelf front show more PSW sinking to the bottom over the entire ice shelf front in B3 than B4 and B1 (Fig. 10), consistent with the higher density of polynya bottom water in B3 than B4 and B1 on both day 40 (Fig. 5d versus Fig. 6d; B1 not shown) and day 100 (Fig. 8b versus Figs. 8d and 8f).

To examine the representativeness of this bottom density comparison over the simulation period, we compare the time evolution of polynya bottom density averaged in the box at the ice tongue end corner in the first 100 days in B1, B3, and B4 (Fig. 11a). After the initial adjustment, the bottom density in B3 is persistently the highest, B4 has an intermediate bottom density, and B1 has the lowest bottom density. This confirms that B3 has the highest polynya destratification rate, followed by B4 and then B1.

b. *Dynamics of PSW circulation*

Here we investigate the mechanism behind the differences in the modeled polynya destratification rates. First, we compare the surface buoyancy fluxes in the simulations to examine whether the differences result from variations in the PSW source. Both B1 and B3 have a similar pattern of surface freshwater flux into the ocean as in B4 (Fig. 12a). Time evolution of the averaged freshwater flux in the polynya region is similar in B1, B3, and B4 (Fig. 12b), despite small-amplitude oscillations in B4 caused by oscillations of the vortex (see section 3c). This similarity is not surprising as the atmospheric forcings in these simulations are the same and the polynya areas are very similar. Therefore, adding the ice tongue or the headland does not change the surface buoyancy flux in the polynya region, and differences in the PSW flows in the simulations are likely caused by variations in the modeled polynya circulations.

As shown in Part I, polynya circulation is largely driven by winds. Runs B1, B3, and B4 are forced by the same winds and have the same pattern of surface stress curl with a positive (negative) curl on the western (eastern) edge of the wind forcing region (Fig. 13). The circulation differences among B1, B3, and B4 are thus caused by different modulation of the ocean response to the wind forcing. In B1, with no ice tongue or headland, positive and negative relative vorticity appears on the west and east sides of the polynya outflow, respectively (Fig. 13b), corresponding to the aforementioned anticyclonic and cyclonic flow pattern (Fig. 5 in Part I). This dipole flow pattern could be attributed to convergence and divergence of the surface Ekman transport to the west and east of the wind forcing region, respectively. Close examinations of the model results show that they drive sea level setup and setdown on the west and east sides of the offshore plume, respectively (not shown), which, through geostrophic balance, drives the anticyclonic and cyclonic flows. The vorticity of these flows originates from the positive and negative wind stress curl in the wind forcing region (Fig. 13a). From the perspective of vorticity balance, as shown below with B4 as an example, the wind-driven plume outflow transports the positive and negative vorticity generated in the polynya region by the wind stress curl offshore. Once leaving the forcing region, the flow loses the vorticity injection from the wind and starts to respond to the vorticity. That is, the positive (negative) vorticity to the west (east) of the polynya starts to rotate the flow counterclockwise (clockwise) and form the large dipole flow pattern, which includes the eastward (westward) coastal compensating flow to the west (east) of the polynya (Figs. 8a,b). Model

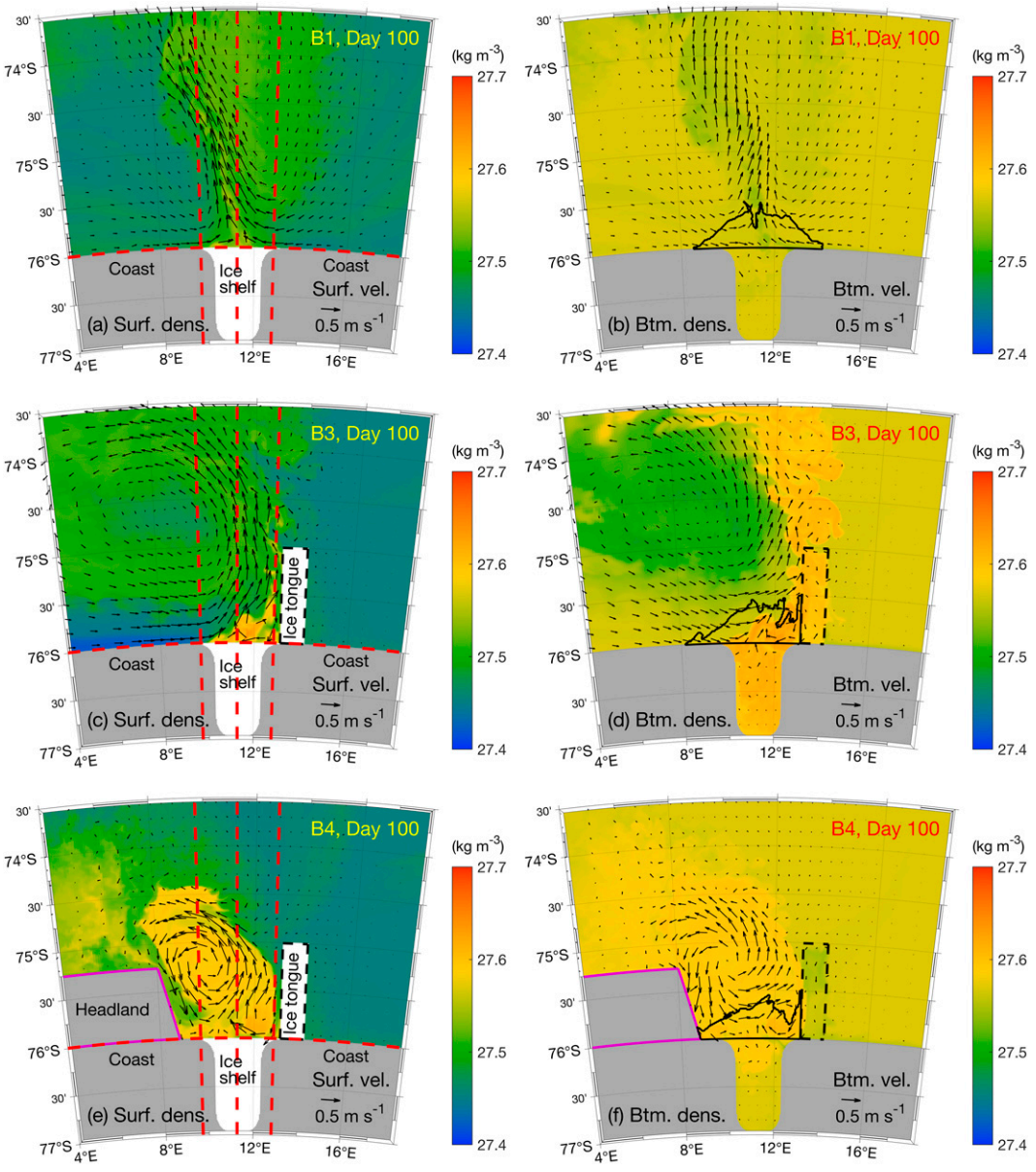

FIG. 8. Snapshots of potential density (color) and velocity (arrows) at the (left) surface and (right) bottom on day 100 from Runs (a),(b) B1, (c),(d) B3, and (e),(f) B4. Black lines in (b), (d), and (f) outline the surface area of the coastal polynya on day 100. The red dashed lines represent three cross-shelf transects in the west end, middle, and east end of the polynya, and the along-coast transects near the ice shelf front.

diagnostics (not shown) indicate that the momentum of the eastward and westward coastal flows is in a rough balance, which keeps the polynya outflow along the centerline of the ice shelf before the Coriolis force pushes the outflow to the west.

In B3, the ice tongue blocks the flow and clockwise rotation on the east side of the polynya, and only the positive relative vorticity to the west of the polynya can rotate the velocity and form the anticyclonic vortex (Fig. 13d). This causes an asymmetrical flow pattern across the polynya outflow. As a result, the eastward coastal return flow to the west of the polynya is the only flow compensating for the polynya outflow and thus greatly strengthened compared to that in B1 (Figs. 8a–d). This strong coastal flow pushes the polynya outflow eastward against the ice tongue. There is no room for any return flow to develop to the east of the polynya outflow. The counterclockwise turning of the flow in the anticyclonic vortex from the eastward coastal current to the offshore outflow creates a wedge at the ice tongue end corner with a negative relative vorticity. The cyclonic flow inside the wedge is separated from the polynya outflow, which traps and then accumulates some of the PSW. Because this part of the PSW is not carried

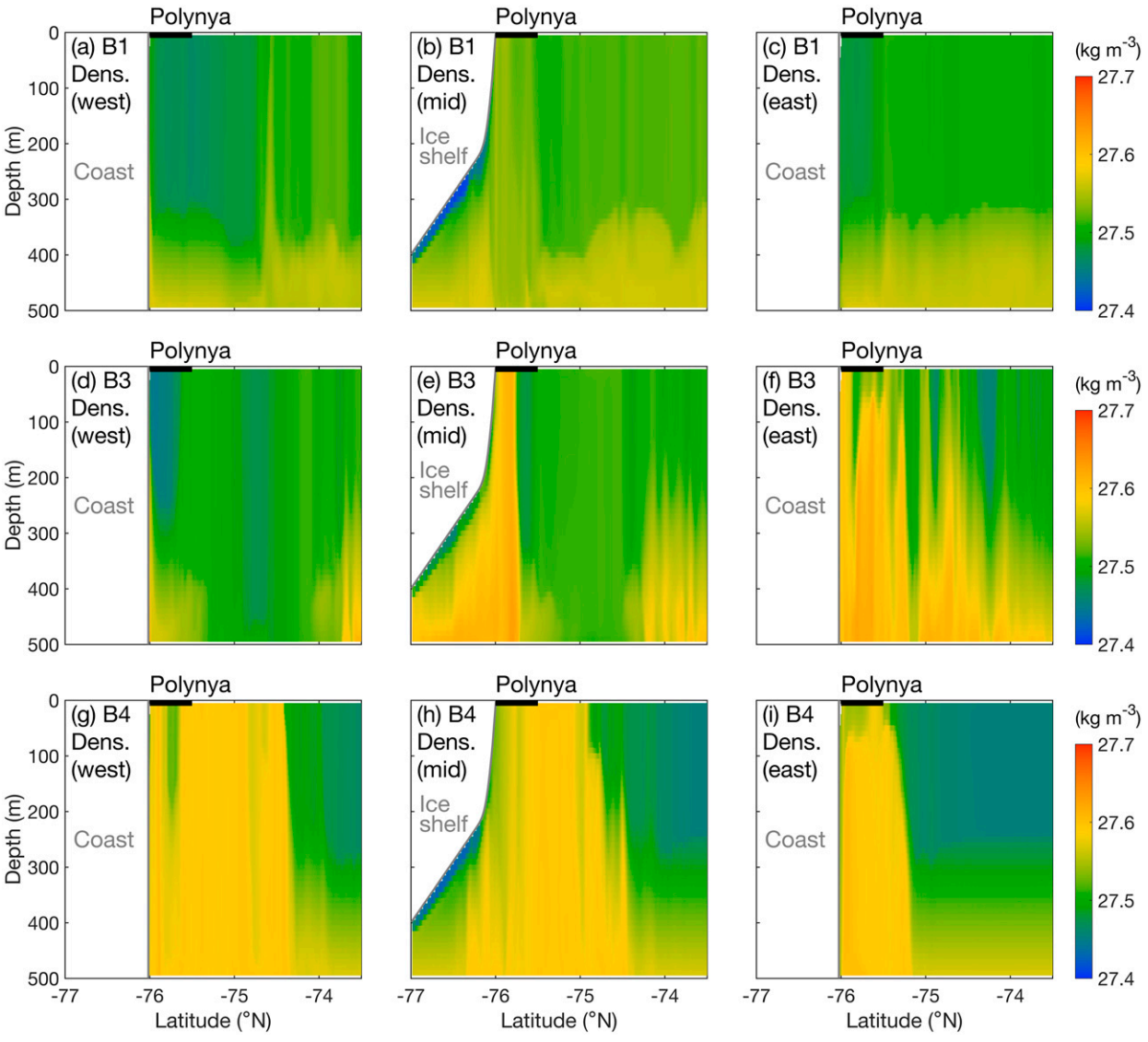

FIG. 9. Cross sections of potential density on day 100 along the three red dashed cross-shore lines in (a)–(c) Fig. 8a for Run B1, (d)–(f) Fig. 8c for Run B3, and (g)–(i) Fig. 8e for Run B4.

offshore by the offshore plume, it sinks quickly and breaks down the water-column stratification in the corner efficiently. This differs from B1, where the polynya circulation is more symmetric with coastal compensating flows from both the west and east meeting in the middle of the ice shelf front, which causes more PSW to be transported away from the polynya region by the outflow and thus suppresses local sinking of the PSW.

The blocking effect of the ice tongue changes with the ice tongue length. Runs B3-IT with ice tongues of different lengths show a dramatic increase of the bottom density at the ice tongue end corner on day 80–100 when the ice tongue length increases from 45 to 55 km (Fig. 11b). The modeled bottom density changes very little when the ice tongue is shorter than 45 km or longer than 55 km. The ice tongue length at which the transition occurs coincides with the cross-shore width of the polynya, ~45 km (Fig. 8d). Close examination of the B3-IT simulations shows that, when the ice tongue is shorter than the polynya width (Figs. 14a,b), the flow to the east of the polynya outflow is not effectively blocked, and a westward current forms at the northern end of the ice tongue, which pushes the polynya outflow slightly westward away from the ice tongue. This allows a southward current to develop in the space between the ice tongue and the polynya. The southward flow transports water from the east into the polynya region and compensates for part of the polynya outflow. This prevents the formation of a large stagnant wedge area in the ice tongue end corner, and the local sinking of the PSW in the corner is thus suppressed. When the ice tongue is longer than the polynya width (Figs. 14c,d), the water supply

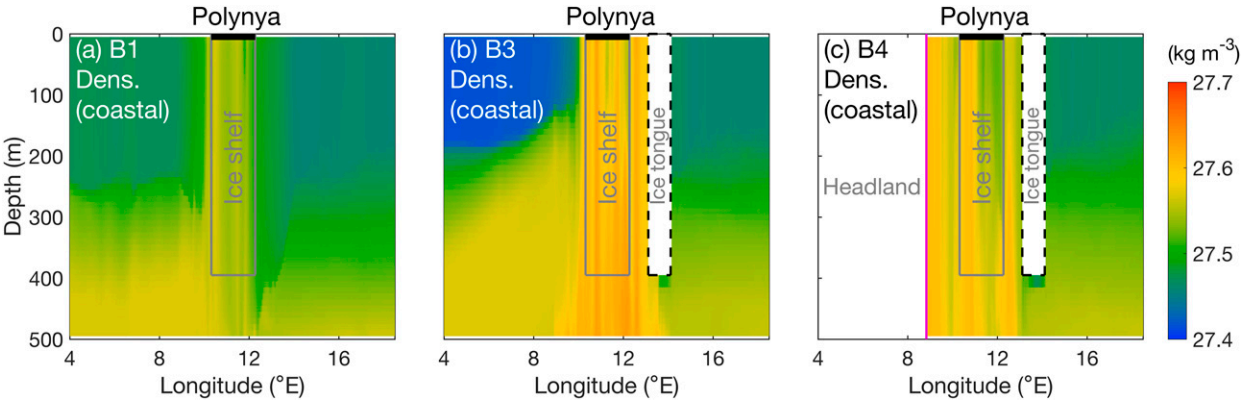

FIG. 10. Cross sections of potential density on day 100 along the red dashed along-coast lines in (a) Fig. 8a for Run B1, (b) Fig. 8c for Run B3, and (c) Fig. 8e for Run B4.

from the east to the polynya region is almost entirely blocked, and the polynya outflow is pushed against the ice shelf as in Run B3. Further extending the ice tongue does not significantly change the polynya circulation. These confirm that blocking of the coastal compensating flow from the east into the polynya by the ice tongue reduces offshore transport of the PSW, enhances local sinking of the PSW, and accelerates destratification of the polynya water column.

In B4, the headland blocks the large-scale circulation to the west of the polynya and restricts the region of the anticyclonic flow (Fig. 8e). It causes the anticyclonic vorticity to concentrate in a small region to the immediate east of the headland (Fig. 13f), which resembles the observed vortex in the TNBP (Figs. 1c–h). To understand the associated vorticity dynamics, we diagnose the vorticity budget in the B4 model. Two locations (Fig. 13f), one in the anticyclonic vortex under the influence of strong surface stress curl (box A) and the other in the offshore plume without the influence of strong surface stress curl (box B), are selected to calculate the terms in the volume-averaged vorticity equation:

$$\frac{\partial \overline{\zeta}}{\partial t} = \overline{-(\zeta + f)\left(\frac{\partial u}{\partial x} + \frac{\partial v}{\partial y}\right)} + \overline{\left(-u\frac{\partial \zeta}{\partial x} - v\frac{\partial \zeta}{\partial y}\right)} + \overline{\frac{1}{\rho_0 h_N}\left(\frac{\partial \tau_{sy}}{\partial x} - \frac{\partial \tau_{sx}}{\partial y}\right)} + \overline{\frac{1}{\rho_0 h_N}\left(\frac{\partial \tau_{by}}{\partial x} - \frac{\partial \tau_{bx}}{\partial y}\right)} + \overline{\kappa_H\left(\frac{\partial^2 \zeta}{\partial x^2} + \frac{\partial^2 \zeta}{\partial y^2}\right)} + \overline{\frac{\partial w}{\partial y}\frac{\partial u}{\partial z} - \frac{\partial w}{\partial x}\frac{\partial v}{\partial z} - w\frac{\partial \zeta}{\partial z}}. \quad (1)$$

Here, ζ is relative vorticity of the horizontal flow, f is the Coriolis parameter, u is zonal velocity, v is meridional velocity, w is vertical velocity, h_N is the water depth, ρ_0 is the reference density of seawater; τ_{sx} (τ_{sy}) and τ_{bx} (τ_{by}) are the surface and bottom stress in the zonal (meridional) direction, respectively; κ_H is the horizontal viscosity; the overbar indicates volume averaging. The terms on the right-hand side of (1) represent vorticity horizontal divergence, horizontal advection, source from the surface stress curl, source from the bottom stress curl, horizontal diffusion, and the curl of the vertical advection term in the horizontal momentum equation, respectively.

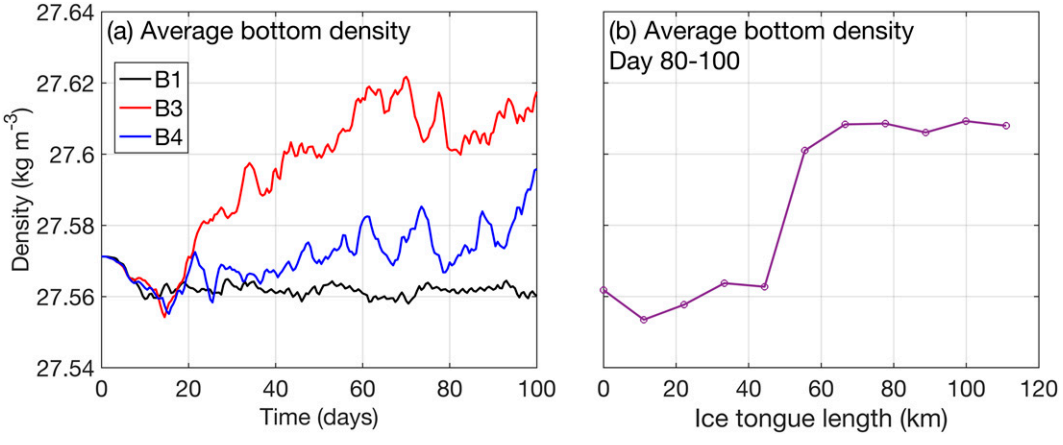

FIG. 11. (a) Time evolution of the averaged bottom density at the ice tongue end corner (the blue box in Figs. 5d and 6d) in Runs B1, B3, and B4. (b) Mean bottom densities at the ice-tongue-polynya corner in day 80–100 in Runs B3-IT with different ice tongue length.

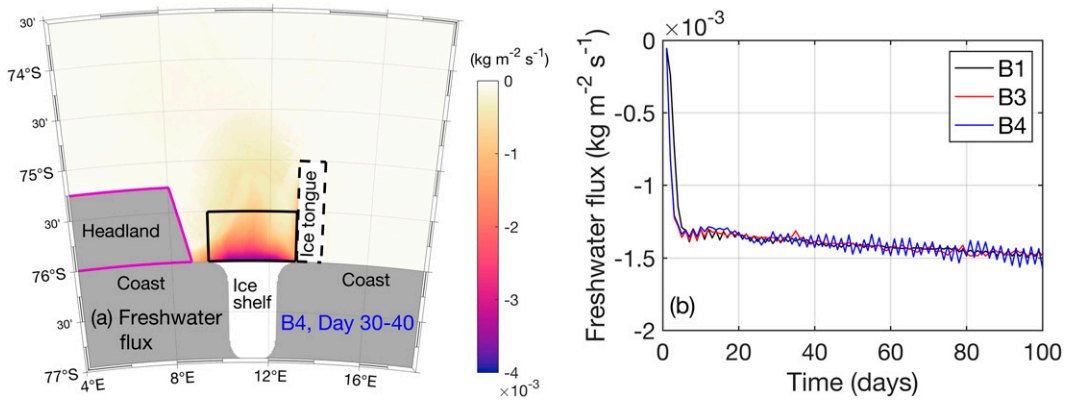

FIG. 12. (a) Net surface freshwater flux into the ocean averaged over day 30–40 in Run B4; (b) time evolution of the net surface freshwater flux averaged within the black box outlined in (a) in Runs B1, B3, and B4. Note that negative freshwater flux means increasing salinity in the ocean.

The vorticity diagnostics show that the dominating terms in the vorticity balance change spatially. Within box A (Fig. 15a), the major vorticity balance is between the surface and bottom stress curl, especially later in the simulation when the system reaches a quasi-equilibrium state. The other terms are generally secondary. This indicates that vorticity within the anticyclonic vortex is mainly driven by the surface stress curl. In contrast, within the offshore box B (Fig. 15b) where the surface stress is only generated by flows of the sea ice and thus weak, the main vorticity balance is between the lateral advection, i.e., upstream injection, and the horizontal divergence term. The net advective flux convergence of vorticity in the box is thus negligible. Detailed analysis of the model results shows that horizontal divergence of the vorticity results from the small-scale covariance between the vorticity and divergence of the horizontal flow, which serves as a sink of the total relative vorticity in the system.

In B4, the headland also blocks the eastward coastal current. Consequently, the polynya outflow is not pushed against the ice tongue as in B3, and a narrow southward current forms between the ice tongue and the polynya outflow, reaching the ice tongue end corner (Fig. 8e). This southward current to the east of the polynya outflow, together with the southeastward current on the southwest edge of the anticyclonic vortex, volumetrically compensate for the polynya outflow. Essentially, the addition of the headland to the west of the polynya causes the polynya circulation in B4 to be more symmetric than that in B3. The compensating flow to the east of the polynya pushes some of the PSW in the ice tongue end corner into the polynya outflow, suppresses local sinking of the PSW, and slows down the destratification of the polynya water column. All these suggest that coastal geometry influences polynya water-column destratification through modifying polynya circulation and offshore transport of the PSW.

c. *Temporal variation*

To further reveal the connection among polynya circulation, offshore transport of the PSW, and polynya water-column destratification, we compare the offshore volume transport and the associated offshore loss of the PSW in Runs B1, B3, and B4. Vertically and zonally integrated fluxes of total water volume, PSW passive tracer, and density anomaly across an alongshore transect immediately offshore of the polynya (orange lines in Figs. 5e and 6e) are obtained from the simulations (Fig. 16). All fluxes exhibit oscillation with a period of 2 days, consistent with the prescribed wind fluctuation. The fluxes in B4 also exhibit strong variation on the time scale of 10–15 days. We here start with comparing temporal mean fluxes in the simulations and will analyze the strong temporal variation in B4 later in this section.

Without the ice tongue or headland (B1), the temporal mean volumetric flux of the polynya outflow is the highest. It is consistent with the water supply from the coastal currents on both sides of the polynya. The mean offshore volume flux is reduced in B3 when the ice tongue is included, which blocks the coastal compensating flow from the east. B4 has the lowest mean offshore volume flux because coastal currents on both sides are mostly blocked and replaced by weaker southward compensating flows.

The modeled PSW and density anomaly fluxes across the alongshore transect exhibit a different behavior than the volume fluxes. Among the 3 runs, B3 has the lowest mean PSW offshore flux, which is consistent with B3 having the highest amount of PSW sinking locally in the polynya water column and the fastest polynya destratification. Interestingly, B4 has the highest mean PSW and density anomaly offshore fluxes, despite the mean offshore volume flux being the lowest. Close examination of the model solution suggests that it results from much of the PSW being trapped in the anticyclonic vortex, which causes some PSW to be carried southward across the alongshore transect back to the source region by the vortex flow (Figs. 8e,f). Trapping of the PSW in the anticyclonic vortex in B4 is caused by wind-induced convergence of surface Ekman flow and then Ekman pumping, i.e., downwelling, at the vortex center. The convergent flow entrains surface waters from the surrounding area toward the vortex center and then carries it downward. This causes water at the vortex

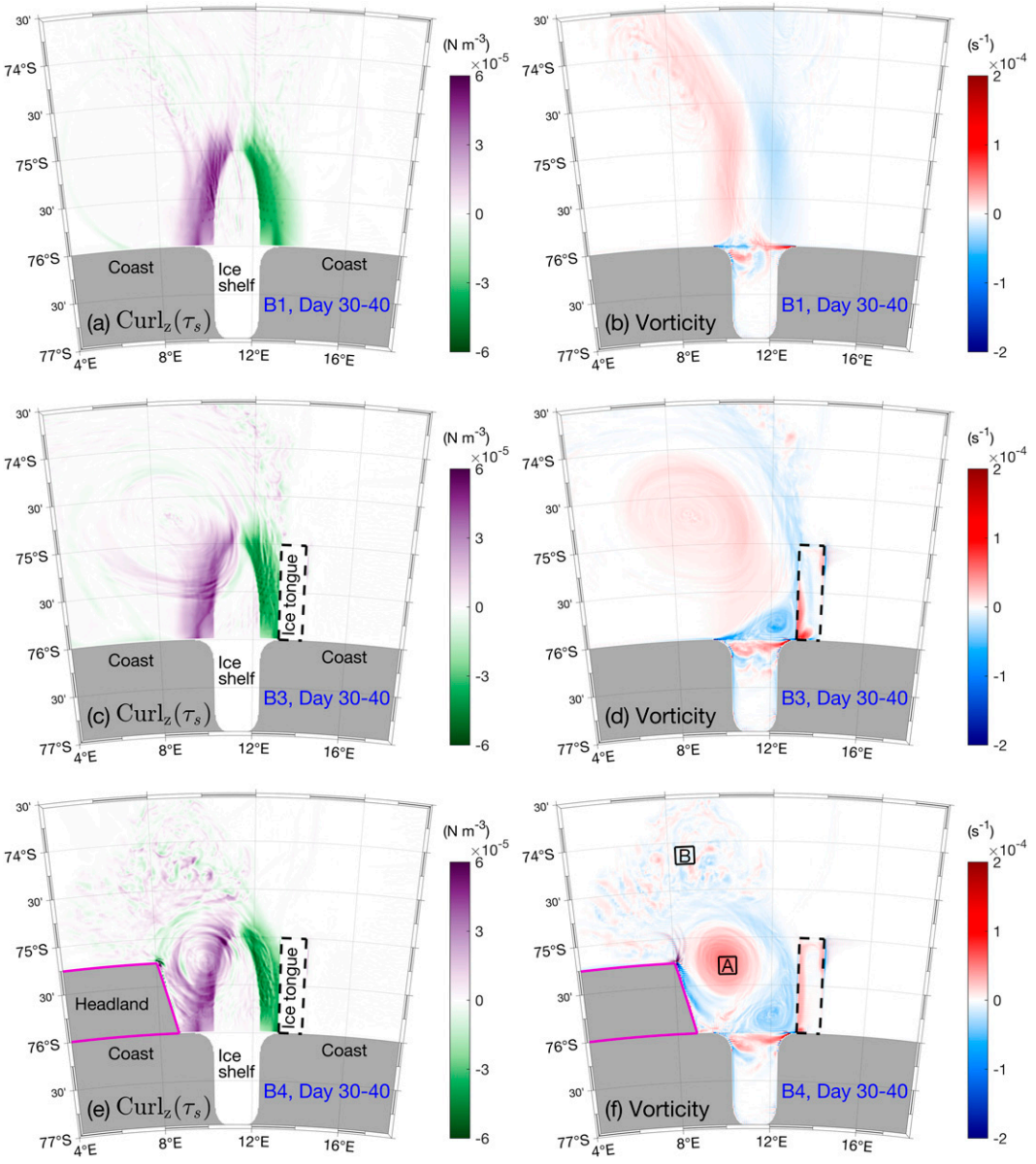

FIG. 13. (left) Curl of the ocean surface stresses and (right) water-column-averaged relative vorticity averaged over day 30–40 in Runs (a),(b) B1, (c),(d) B3, and (e),(f) B4. The black boxes in (f) indicate the regions A and B where the terms in the vorticity equation are averaged and plotted in Fig. 15.

center to transition from low density on day 40 (Figs. 6c,d) to high density on day 100 (Figs. 8e,f). Essentially, as time proceeds, the downward flow in the vortex center switches from carrying the originally lower-density surface water to carrying high-density PSW to the bottom layer. Correspondingly, diagnostics of the horizontal divergence term in the model (not shown) indicate that there is a divergent flow at the vortex bottom (Fig. 6d), presumably resulting from the outward bottom Ekman transport induced by the bottom stress. Ekman pumping of the PSW into the vortex is also consistent with the slower polynya destratification in B4 relative to B3. Entrainment of the PSW into the vortex reduces the amount of PSW sinking in the polynya source region. However, the downwelling flow at the vortex center represents another mechanism of ventilating the bottom layer of the Antarctic continental shelf occurring outside of coastal polynyas. As this study focuses on the water column destratification in the polynya, we leave the influence of the vortex Ekman pumping on the bottom shelf water for future studies.

Strong variation of the offshore fluxes in B4 on the time scale of 10–15 days results from instability of the vortex flow that deforms the vortex and then the polynya outflow. Here, we highlight the polynya circulation on two different days,

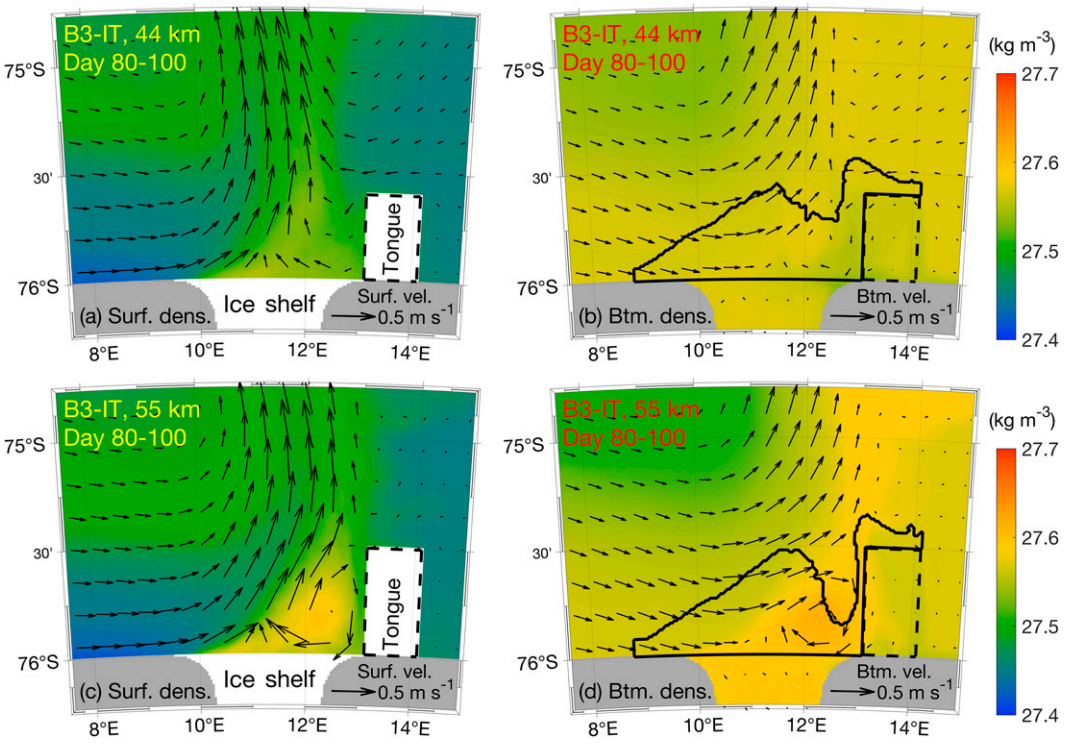

FIG. 14. Potential density (color) and velocity (arrows) at the (left) surface and (right) bottom averaged over day 80–100 in two of Runs B3-IT where ice tongue lengths are (a),(b) 44 and (c),(d) 55 km.

day 63 and 87, when the offshore fluxes reach a maximum and minimum, respectively (Fig. 16). Modeled solutions on both days show an elongated vortex pattern (Fig. 17). On day 63, the long axis of the vortex aligns with the cross-shore direction, which gives a large offshore velocity component across the transect. This drives the large offshore volume and PSW transport on that day. On day 87, the long axis of the elongated vortex is oriented alongshore, parallel to the transect.

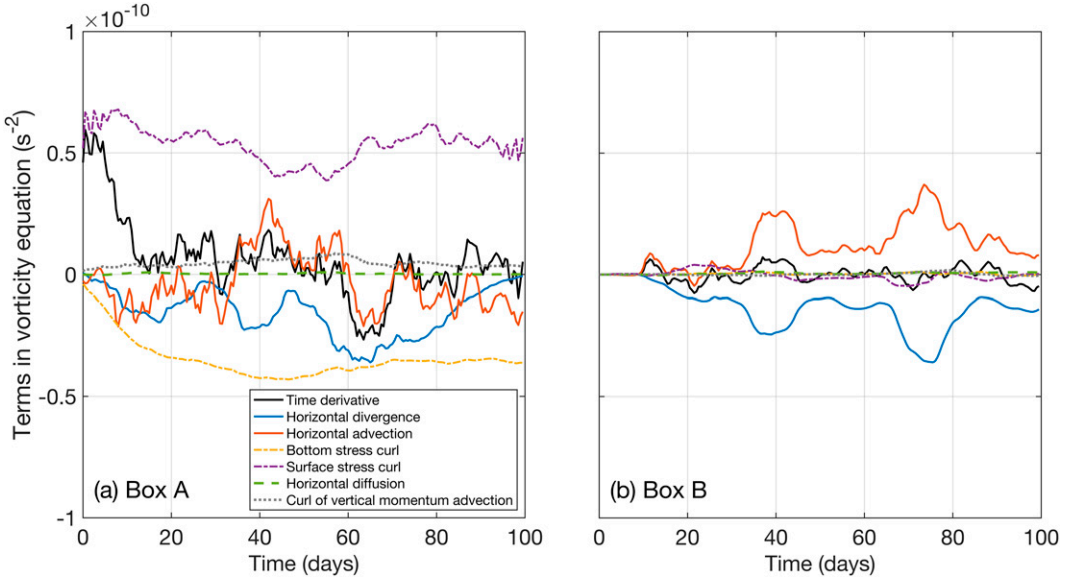

FIG. 15. Time series of the terms in the volume-averaged vorticity equation in run B4 within (a) a nearshore box A and (b) an offshore box B, as labeled in Fig. 13f. The time series here have been smoothed with a 10-day running window.

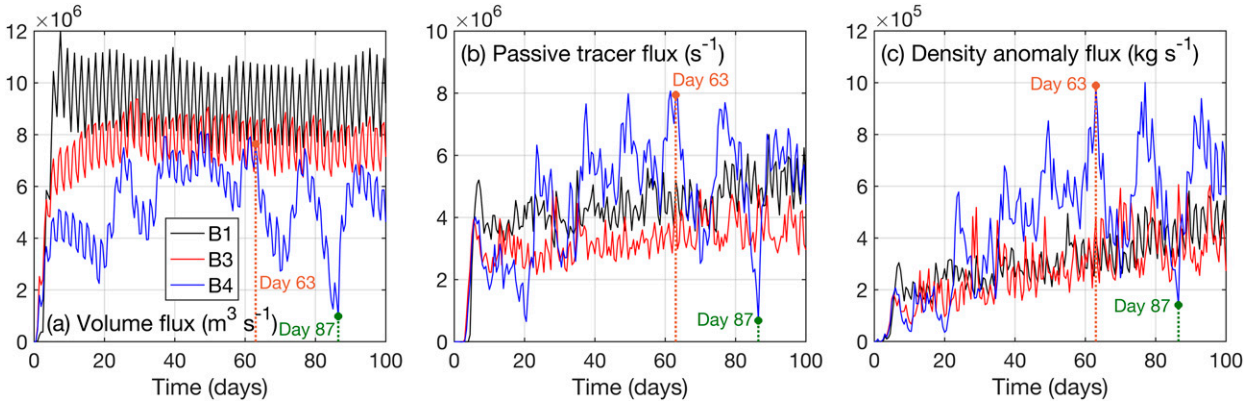

FIG. 16. Integrated (a) volume, (b) passive tracer, and (c) density anomaly fluxes across the transects along the orange lines in Figs. 5e and 6e for Runs B1, B3, and B4. Day 63 and day 87 are highlighted with dotted lines.

As a result, the velocity component normal to the transect is weak and fluxes across the transect are minimal. Detailed examination of the B4 solution shows that the vortex deformation occurs over much of the water column. It results from the instability of the vortex and causes periodical oscillation in the vortex flow. It generates the 10–15-day oscillation of the fluxes in the later part of the simulation (Fig. 16). The time scale of this vortex instability is consistent with the advection time scale of the vortex flow. Given a mean radius of the vortex of ~55 km and a mean flow of 0.3–0.4 m s^{-1}, it takes 10–14 days for the flow to make a complete circle around the vortex. Therefore, the vortex instability likely results from advective resonance of the flow disturbance induced by the fluctuating winds. That is, wind-induced flow disturbances on the time scale of 10–14 days (multiple of the wind periods) are amplified by the recirculation of the disturbance around the vortex. Note that the observed vortex at the TNBP also exhibits deformation on the time scale of several days (Figs. 1c–f). The correspondence between this variation of the polynya circulation and the PSW outflow, and the connection between the outflow and destratification confirm that coastal geometry plays a prominent role in regulating water-column stratification and PSW circulation in a polynya region.

4. Discussion

With the idealized model setup, we have qualitatively demonstrated the impacts of an ice tongue and a headland on PSW circulation and destratification in polynyas. In the ocean, other physical factors, including those examined in Part I, may interact with coastal geometry and further complicate the polynya circulation. Here, we use alongshore wind as a demonstration. In particular, we examine additional simulations, B2, B5, and B6 (Fig. 18), in which an alongshore easterly wind with a speed of $U_a = 10$ m s^{-1} is added to B1, B3, and B4, respectively. Part I shows that, without the ice tongue or the headland, alongshore coastal easterly winds U_a can affect polynya destratification through inducing onshore Ekman transport and reducing the offshore export of the PSW. With the ice tongue and the headland, the influence of alongshore winds is qualitatively similar. In particular, on day 100, modeled surface flows veer westward, and modeled bottom density in the polynya and ice shelf cavity region is higher

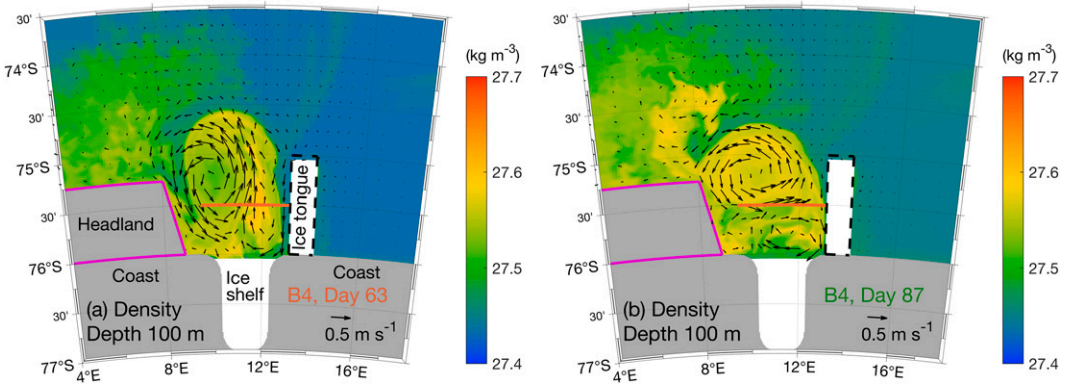

FIG. 17. Snapshots of potential density (color) and velocity (arrows) at 100-m depth in Run B4 on day 63 and day 87, corresponding to the times of maximum and minimum cross-shore fluxes (Fig. 16b), respectively. The orange lines in both panels indicate the transect where integrated offshore fluxes are shown in Fig. 16.

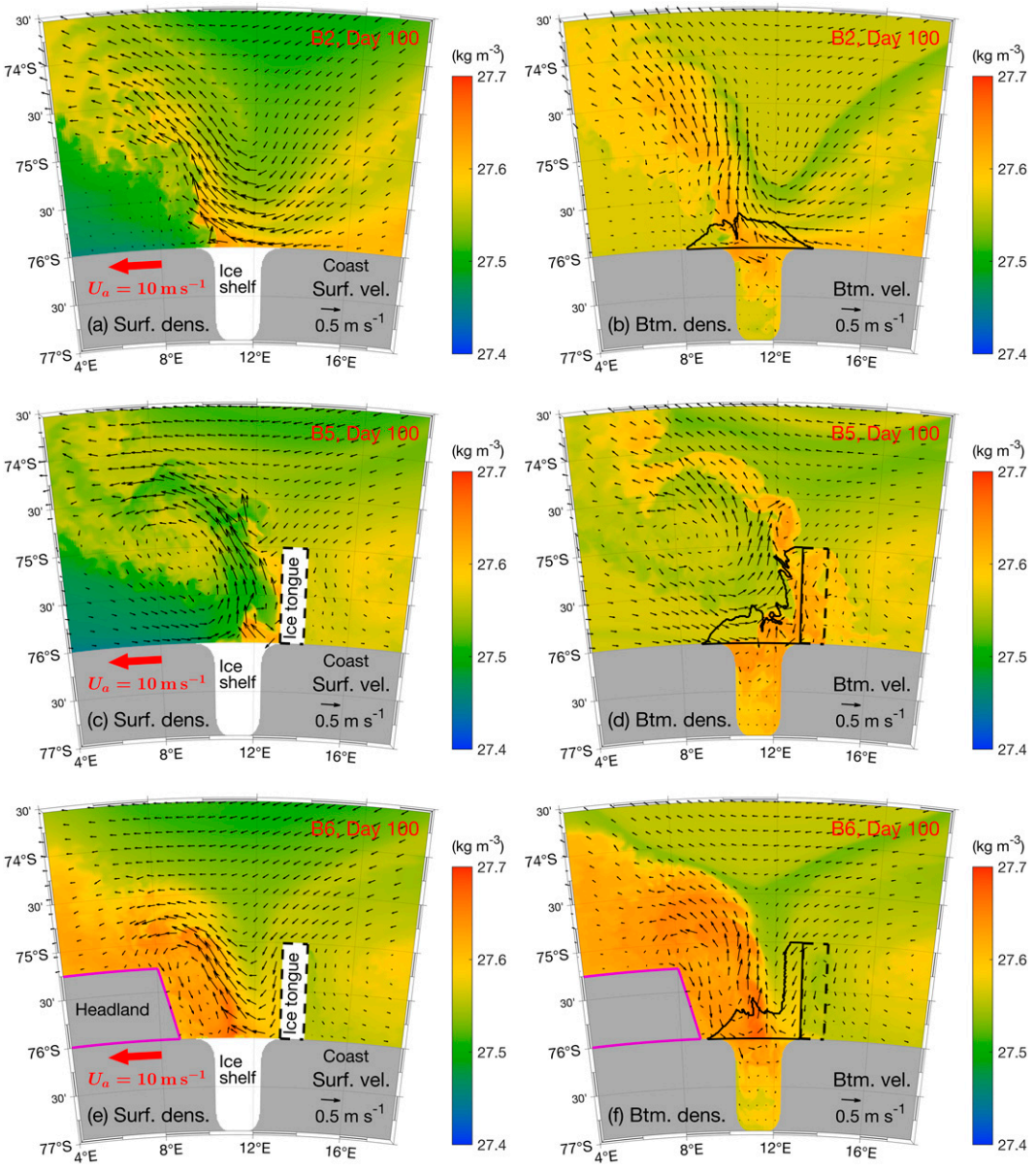

FIG. 18. Snapshots of potential density (color) and velocity (arrows) at the (left) surface and (right) bottom on day 100 from Runs (a),(b) B2, (c),(d) B5, and (e),(f) B6. Black solid lines in (b), (d), and (f) outline the coastal polynya on day 100.

in B2, B5, and B6, compared to B1, B3, and B4, respectively. Therefore, the Ekman dynamics as explained in Part I is still applicable, and polynya water column destratification is accelerated with the addition of alongshore easterly winds. Meanwhile, bottom densities in the ice shelf cavity in B5 and B6 are also higher than in B2 with no ice tongue or headland. This indicates that the influence of the ice tongue and headland on the PSW circulation has not been fundamentally altered by the alongshore easterly winds.

The alongshore easterly winds can alter the details of the coastal circulation and affect the overall transport of the PSW. For instance, when an ice tongue and alongshore easterly winds are both present, a polynya is formed in the lee of the ice tongue in both B5 and B6 (Figs. 18d,f). In these cases, the ice tongue helps to enhance the sea ice production and PSW formation by expanding the area of the polynya, which is consistent with findings of previous studies (Kurtz and Bromwich 1985; Ohshima et al. 2013; Williams et al. 2010). Runs B5 and B6 also give drastically different density distribution with B6 showing much more PSW being trapped in the larger polynya-vortex region. This indicates that the onshore Ekman transport induced by the easterly winds can interact with the headland to the west of the polynya and efficiently trap much of the PSW in the polynya-vortex region.

As a result, the amount of PSW leaving this coastal region is much less in B6 than in B5, resulting in a slightly higher maximum density of PSW at the bottom in B6 than in B5 (Figs. 18d,f), whereas the opposite is true in the same geometric setup but without easterly winds (PSW density at the bottom is lower in B4 than in B3; Fig. 8). These suggest that details of the configurations in a coastal polynya have a significant influence and should be considered when studying the dispersal of PSW.

The fundamental processes of coastal geometry affecting polynya circulation and stratification illustrated in this study are applicable not only to the TNBP but also to other coastal polynyas with complex geometry, such as ice tongues and headlands. For instance, the B3-IT simulations with altered ice tongue lengths may be used to explain the significant reduction in DSW export in the Mertz Polynya after its calving event in 2010 (Lacarra et al. 2014; Snow et al. 2018). Assuming that the Mertz Glacier Tongue keeps a growth rate of $\sim$1 km yr^{-1} (Giles 2017) and the offshore width of the Mertz Polynya is $\sim$40 km similar to our modeled polynya, the restoration of DSW export from the Mertz Polynya to a level comparable to that prior to its 2010 calving event shall be expected within $\sim$40 years, when the Mertz Glacier Tongue exceeds the offshore width of the Mertz Polynya. Moreover, the case with the ice tongue and alongshore easterly winds (B5) can qualitatively represent Cape Darnley Polynya, where coastal easterly winds are prominent and the sea ice inflow from the east has been blocked by a grounded iceberg (Nihashi and Ohshima 2015; Ohshima et al. 2013). Consistently, through analyzing wintertime hydrographic measurements in the Cape Darnley Polynya in 2017, Aoki et al. (2020) suggested that local three-dimensional DSW circulation might affect salinity evolution in the polynya water column.

The processes described here may explain differences in DSW formation among Antarctic coastal polynyas. For instance, the coastal polynyas that are known to be sources of the DSW and AABW, such as the TNBP, the Mertz Polynya, the Vincennes Bay Polynya, and the Cape Darnley Polynya (Budillon and Spezie 2000; Kitade et al. 2014; Ohshima et al. 2013; Rusciano et al. 2013; Williams et al. 2010), are often affiliated with ice tongues or similar features. Presumably, the neighboring ice tongues or icebergs enhance local sinking of the PSW in the polynyas and facilitate formation of the DSW, which then flows offshore, supplying AABW.

5. Summary

This study shows that coastal geometry can substantially affect the destratification rate in coastal polynyas. Even with the same polynya size and the same rate of PSW production at the polynya surface, the coastal circulation and water column destratification processes vary significantly across simulations with and without an ice tongue or a headland (section 3; Figs. 8, 9 and 10). Besides impeding sea ice flow into the polynya at the ocean surface, an ice tongue can block water column circulation on one side of the polynya and cause the polynya outflow to abut the ice shelf (Fig. 5). This creates a relatively stagnant wedge region at the corner between the ice shelf and the ice tongue, which reduces offshore loss of the PSW, enhances local sinking of the PSW in the polynya, and then accelerates the destratification of the polynya water column. A headland on the other side of the polynya can also alter the three-dimensional PSW dispersal by restoring the alongshore symmetry of the polynya circulation (Fig. 6). The headland causes the polynya outflow to separate from the ice tongue and allows ambient water to flow along the ice tongue to compensate for the polynya outflow. This process enhances the offshore transport of the PSW and slows down polynya water-column destratification. Meanwhile, simulations with different ice tongue lengths demonstrate that the ice tongue's blocking effect is only effective when the ice tongue is longer than the cross-shore width of the polynya (Fig. 14). Adding the headland to the other side of the polynya generates an intense vortex (Fig. 13f), which resembles observations in the TNBP (Figs. 1c–h). Instability of the vortex flow drives strong temporal variability in the polynya outflow, which affects the export of PSW from the polynya region and polynya destratification (Figs. 16 and 17). All these results indicate the importance of considering small-scale icescape and coastline geometry in studies of polynya stratification and PSW circulation.

Part I of this study shows that alongshore easterly winds can suppress offshore transport of PSW and enhance polynya destratification through onshore Ekman transport. This Part II work further demonstrates that besides the circulation barrier induced by the winds in Part I, physical barriers such as a neighboring ice tongue can also modify the circulation and accelerate water column destratification in the polynya. Together, these studies highlight the impacts of a variety of physical factors, such as wind strength, wind direction, air temperature, initial ambient stratification, water depth, ice tongues, and coastal geometry on polynya water column destratification. The influences of other factors remain to be explored, e.g., land-fast ice, bathymetric variations, onshore intrusion of the offshore warm Circumpolar Deep Water, ice shelf melting, and shape and location of the continental shelf. In addition, variations of the polynya stratification due to changes in factors such as breaking of the ice tongue and land-fast ice and the associated relocation or size change of the polynyas also need to be investigated in future studies.

Despite these limitations, we have demonstrated with high-resolution idealized numerical models that altering local forcing and geometric features such as ice tongues can modify the polynya circulation and lead to substantial changes in the rate of polynya destratification and pathways of the PSW dispersal. Only when a polynya water column is completely mixed, part of the PSW formed on the polynya surface can sink directly down to the bottom and become DSW, which then propagates offshore on the seafloor across the shelf edge supplying AABW. Because the winter season has a limited length and the water column tends to restratify in the summer, the time it takes the polynya water column to be completely mixed determines whether a polynya can form DSW and supply AABW. Hence, the rate of destratification studied here is essential for determining the amount of DSW formed in a particular polynya and then exported to the deep

ocean supplying AABW. Understanding impacts of the physical factors in a coastal region on the PSW circulation and destratification in polynyas is vital to understanding the AABW formation and global ocean water mass distribution. For instance, the presence of alongshore easterly winds and an ice tongue at a polynya would increase the amount of DSW formed in the polynya to supply AABW. Future modeling studies of the large-scale AABW formation should either resolve or parameterize these local influences.

Acknowledgments. This study is supported by the National Science Foundation through Grants OPP-1643735, OPP-1643901, and OPP-2021245. YX and WGZ are also supported by OPP-2205008. We thank Dr. Peter Guest for sharing the atmospheric data measured during the PIPERS expedition.

Data availability statement. The MODIS image was obtained from the Worldview tool from NASA's Earth Observing System Data and Information System at https://worldview.earthdata.nasa.gov/. The Sentinel-1 image processed by ESA was downloaded from NASA's Distributed Active Archive Centers operated by the Alaska Satellite Facility at https://asf.alaska.edu/. The meteorological station data were downloaded from the University of Wisconsin-Madison Automatic Weather Station Program at https://amrc.ssec.wisc.edu/. The PIPERS CTD data were obtained from the U.S. Antarctic Program Data Center at https://www.usap-dc.org/view/dataset/601422. The model code and scripts used to conduct the simulations and analyses in this study are available at https://doi.org/10.5281/zenodo.7761706.

REFERENCES

Ackley, S. F., and Coauthors, 2020: Sea-ice production and air/ice/ocean/biogeochemistry interactions in the Ross Sea during the PIPERS 2017 autumn field campaign. *Ann. Glaciol.*, **61**, 181–195, https://doi.org/10.1017/aog.2020.31.

Aoki, S., K. Ono, D. Hirano, and T. Tamura, 2020: Continuous winter oceanic profiling in the Cape Darnley Polynya, East Antarctica. *J. Oceanogr.*, **76**, 365–372, https://doi.org/10.1007/s10872-020-00550-w.

Bromwich, D. H., 1989: Satellite analyses of Antarctic katabatic wind behavior. *Bull. Amer. Meteor. Soc.*, **70**, 738–749, https://doi.org/10.1175/1520-0477(1989)070<0738:SAOAKW>2.0.CO;2.

——, and D. D. Kurtz, 1984: Katabatic wind forcing of the Terra Nova Bay polynya. *J. Geophys. Res.*, **89**, 3561–3572, https://doi.org/10.1029/JC089iC03p03561.

Budillon, G., and G. Spezie, 2000: Thermohaline structure and variability in the Terra Nova Bay polynya, Ross Sea. *Antarct. Sci.*, **12**, 493–508, https://doi.org/10.1017/S0954102000000572.

Dinniman, M. S., P. St-Laurent, K. R. Arrigo, E. E. Hofmann, and G. L. van Dijken, 2020: Analysis of iron sources in Antarctic continental shelf waters. *J. Geophys. Res. Oceans*, **125**, e2019JC015736, https://doi.org/10.1029/2019JC015736.

Frezzotti, M., and M. C. G. Mabin, 1994: 20th century behaviour of Drygalski ice tongue, Ross Sea, Antarctica. *Ann. Glaciol.*, **20**, 397–400, https://doi.org/10.3189/1994AoG20-1-397-400.

Giles, A. B., 2017: The Mertz glacier tongue, east Antarctica. Changes in the past 100 years and its cyclic nature – Past, present and future. *Remote Sens. Environ.*, **191**, 30–37, https://doi.org/10.1016/j.rse.2017.01.003.

Guest, P. S., 2021: Inside katabatic winds over the Terra Nova Bay Polynya: 2. Dynamic and thermodynamic analyses. *J. Geophys. Res. Atmos.*, **126**, e2021JD034904, https://doi.org/10.1029/2021JD034904.

Indrigo, C., C. F. Dow, J. S. Greenbaum, and M. Morlighem, 2020: Drygalski ice tongue stability influenced by rift formation and ice morphology. *J. Glaciol.*, **67**, 243–252, https://doi.org/10.1017/jog.2020.99.

Kitade, Y., and Coauthors, 2014: Antarctic bottom water production from the Vincennes Bay Polynya, East Antarctica. *Geophys. Res. Lett.*, **41**, 3528–3534, https://doi.org/10.1002/2014GL059971.

Kurtz, D. D., and D. H. Bromwich, 1985: A recurring, atmospherically forced polynya in Terra Nova Bay. *Oceanology of the Antarctic Continental Shelf*, S. S. Jacobs, Ed., Antarctic Research Series, Vol. 43, Amer. Geophys. Union, 177–201.

Lacarra, M., M.-N. Houssais, C. Herbaut, E. Sultan, and M. Beauverger, 2014: Dense shelf water production in the Adélie depression, East Antarctica, 2004–2012: Impact of the Mertz glacier calving. *J. Geophys. Res. Oceans*, **119**, 5203–5220, https://doi.org/10.1002/2013JC009124.

Le Bel, D. A., C. J. Zappa, G. Budillon, and A. L. Gordon, 2021: Salinity response to atmospheric forcing of the Terra Nova Bay polynya, Antarctica. *Antarct. Sci.*, **33**, 318–331, https://doi.org/10.1017/S0954102021000146.

Marshall, J., A. Adcroft, C. Hill, L. Perelman, and C. Heisey, 1997: A finite-volume, incompressible Navier stokes model for, studies of the ocean on parallel computers. *J. Geophys. Res.*, **102**, 5753–5766, https://doi.org/10.1029/96JC02775.

Massom, R. A., P. T. Harris, K. J. Michael, and M. J. Potter, 1998: The distribution and formative processes of latent-heat polynyas in East Antarctica. *Ann. Glaciol.*, **27**, 420–426, https://doi.org/10.3189/1998AoG27-1-420-426.

——, K. L. Hill, V. I. Lytle, A. P. Worby, M. J. Paget, and I. Allison, 2001: Effects of regional fast-ice and iceberg distributions on the behaviour of the Mertz Glacier polynya, East Antarctica. *Ann. Glaciol.*, **33**, 391–398, https://doi.org/10.3189/172756401781818518.

Morales Maqueda, M. A., A. J. Willmott, and N. R. T. Biggs, 2004: Polynya dynamics: A review of observations and modeling. *Rev. Geophys.*, **42**, RG1004, https://doi.org/10.1029/2002RG000116.

Nihashi, S., and K. I. Ohshima, 2015: Circumpolar mapping of Antarctic coastal polynyas and landfast sea ice: Relationship and variability. *J. Climate*, **28**, 3650–3670, https://doi.org/10.1175/JCLI-D-14-00369.1.

Ohshima, K. I., and Coauthors, 2013: Antarctic bottom water production by intense sea-ice formation in the Cape Darnley polynya. *Nat. Geosci.*, **6**, 235–240, https://doi.org/10.1038/ngeo1738.

Parmiggiani, F., and C. Fragiacomo, 2005: Cover: The calving event of the Drygalski ice tongue of February 2005. *Int. J. Remote Sens.*, **26**, 4633–4638, https://doi.org/10.1080/01431160500238828.

Randall-Goodwin, E., and Coauthors, 2015: Freshwater distributions and water mass structure in the Amundsen Sea polynya region, Antarctica. *Elementa*, **3**, 0000651, https://doi.org/10.12952/journal.elementa.000065.

Rusciano, E., G. Budillon, G. Fusco, and G. Spezie, 2013: Evidence of atmosphere-sea ice-ocean coupling in the Terra Nova Bay polynya (Ross Sea-Antarctica). *Cont. Shelf Res.*, **61–62**, 112–124, https://doi.org/10.1016/j.csr.2013.04.002.

Silvano, A., S. R. Rintoul, B. Peña-Molino, W. R. Hobbs, E. Van Wijk, S. Aoki, T. Tamura, and G. D. Williams, 2018: Freshening by glacial meltwater enhances melting of ice shelves and reduces formation of Antarctic Bottom Water. *Sci. Adv.*, **4**, eaap9467, https://doi.org/10.1126/sciadv.aap9467.

Snow, K., S. R. Rintoul, B. M. Sloyan, and A. M. C. Hogg, 2018: Change in dense shelf water and Adélie land bottom water precipitated by iceberg calving. *Geophys. Res. Lett.*, **45**, 2380–2387, https://doi.org/10.1002/2017GL076195.

Stevens, C., W. Sang Lee, G. Fusco, S. Yun, B. Grant, N. Robinson, and C. Y. Hwang, 2017: The influence of the Drygalski ice tongue on the local ocean. *Ann. Glaciol.*, **58**, 51–59, https://doi.org/10.1017/aog.2017.4.

Tamura, T., G. D. Williams, A. D. Fraser, and K. I. Ohshima, 2012: Potential regime shift in decreased sea ice production after the Mertz Glacier calving. *Nat. Commun.*, **3**, 826, https://doi.org/10.1038/ncomms1820.

Thompson, L., M. Smith, J. Thomson, S. Stammerjohn, S. Ackley, and B. Loose, 2020: Frazil ice growth and production during katabatic wind events in the Ross Sea, Antarctica. *Cryosphere*, **14**, 3329–3347, https://doi.org/10.5194/tc-14-3329-2020.

Wenta, M., and J. J. Cassano, 2020: The atmospheric boundary layer and surface conditions during katabatic wind events over the Terra Nova Bay polynya. *Remote Sens.*, **12**, 4160, https://doi.org/10.3390/rs12244160.

Williams, G. D., S. Aoki, S. S. Jacobs, S. R. Rintoul, T. Tamura, and N. L. Bindoff, 2010: Antarctic bottom water from the Adélie and George V Land coast, East Antarctica (140–149°E). *J. Geophys. Res.*, **115**, C04027, https://doi.org/10.1029/2009JC005812.

Xu, Y., W. G. Zhang, T. Maksym, R. Ji, and Y. Li, 2023: Stratification breakdown in Antarctic coastal polynyas. Part I: Influence of physical factors on the destratification time scale. *J. Phys. Oceanogr.*, **53**, 2047–2067, https://doi.org/10.1175/JPO-D-22-0218.1.

Yoon, S.-T., and Coauthors, 2020: Variability in high-salinity shelf water production in the Terra Nova Bay polynya, Antarctica. *Ocean Sci.*, **16**, 373–388, https://doi.org/10.5194/os-16-373-2020.